

Radio, X-ray, and γ -ray Emission Models of the Colliding Winds Binary WR 140

J. M. Pittard¹* and S. M. Dougherty²

¹*School of Physics and Astronomy, The University of Leeds, Woodhouse Lane, Leeds LS2 9JT, UK*

²*National Research Council of Canada, Herzberg Institute for Astrophysics, Dominion Radio Astrophysical Observatory, P.O. Box 248, Penticton, British Columbia V2A 6J9, Canada*

Accepted ... Received ...; in original form ...

ABSTRACT

We use hydrodynamical models of the wind-collision region (WCR) in the archetype colliding-wind system WR 140 to determine the spatial and spectral distribution of the radio, X-ray and γ -ray emission from shock accelerated electrons. Our calculations are for orbital phase 0.837 when the observed radio emission is close to maximum. Using the observed thermal X-ray emission at this phase in conjunction with the radio emission to constrain the mass-loss rates, we find that the O-star mass-loss rate is consistent with the reduced estimates for O4-5 supergiants by Fullerton, Massa & Prinja (2006), and the wind momentum ratio, $\eta = 0.02$. This is independent of the opening angle deduced from radio VLBI observations of the WCR that we demonstrate fail to constrain the opening angle.

We show that the turnover at ~ 3 GHz in the radio emission is due to free-free absorption, since models based on the Razin effect have an unacceptably large fraction of energy in non-thermal electrons. We find the spectral index of the non-thermal electron energy distribution is flatter than the canonical value for diffusive shock acceleration (DSA), namely $p < 2$. Several mechanisms are discussed that could lead to such an index. Our inability to obtain fits to the radio data with $p > 2$ does not exclude the possibility of shock modification, but stronger evidence than currently exists is necessary for its support.

Tighter constraints on p and the nature of the shocks in WR 140 will be obtained from future observations at MeV and GeV energies, for which we generally predict lower fluxes than previous work. Since the high stellar photon fluxes prevent the acceleration of electrons beyond $\gamma \gtrsim 10^5 - 10^6$, TeV emission from colliding-wind binary (CWB) systems will provide unambiguous evidence of pion-decay emission from accelerated ions. We finish by commenting on the emission and physics of the multiple wind collisions in dense stellar clusters, paying particular attention to the Galactic Center.

Key words: stars:binaries:general – stars:early-type – stars:individual:WR 140 – stars:Wolf-Rayet – radio continuum:stars – Xrays:stars

1 INTRODUCTION

Massive binary systems containing a Wolf-Rayet (WR) and O-type star often exhibit synchrotron emission arising from relativistic electrons in the presence of a magnetic field (Dougherty & Williams 2000). The non-thermal electrons are widely thought to be accelerated through diffusive shock acceleration (DSA), though other mechanisms are also possible (e.g., Jokipii 1987; Jardine, Allen & Pollock 1996). High-spatial-resolution radio observations (e.g.,

Williams et al. 1997; Dougherty, Williams & Pollacco 2000; Dougherty et al. 2005) have revealed that the acceleration site is the region where the massive stellar winds collide – the wind-collision region (WCR). Thus, colliding-wind binary (CWB) systems present an important laboratory for investigating the underlying physics of particle acceleration since they provide access to higher mass, radiation and magnetic field energy densities than in supernova remnants (SNRs), which have been widely used for such work.

CWB systems are also ideal for understanding related, but more complicated, systems involving colliding winds, such as the cluster of massive stars in the central par-

* E-mail: jmp@ast.leeds.ac.uk

sec of the Galaxy (Ghez et al. 2005), and young, dense stellar clusters (super star clusters), such as the Arches (Figer et al. 1999), NGC 3603 (Moffat et al. 2002), and R136 (Figer, McLean & Morris 1999). Non-thermal radio emission has recently been detected from the Arches cluster (Yusef-Zadeh et al. 2003), and the non-thermal radio filaments and “streaks” near the Galactic Center may have their origin in CWBs and cluster winds (Yusef-Zadeh 2003).

In this paper we model the thermal and non-thermal radio, X-ray and γ -ray emission from one of the most extensively observed CWB systems, WR 140. In Sec. 2 we describe our assumptions for the non-thermal particle spectrum. Sec. 3 contains details of our implementation of the various processes responsible for the non-thermal X-ray and γ -ray emission. Details of the modelling of the radio emission, including several cooling processes, and various emission and absorption mechanisms, can be found in Dougherty et al. (2003) and Pittard et al. (2006). The application of our model to observations of WR 140 is described in Sec. 4, and the implications of our modelling are discussed in Sec. 5. In Sec. 6, we summarize and note future directions.

2 THE NON-THERMAL PARTICLE SPECTRUM AND MAGNETIC FIELD

In this work, it is assumed that the non-thermal particle distribution can be approximated as a power-law $n(\gamma) \propto \gamma^{-p}$, where γ is the Lorentz factor and p is a free-parameter determined from model fits (primarily) to the radio emission. A number of mechanisms can produce such a distribution, as we now discuss along with our assumptions concerning the normalization of the non-thermal particle spectrum and the magnetic field within the WCR.

2.1 Acceleration mechanisms and spectral index of non-thermal particles

There are several possible mechanisms for accelerating particles in CWB systems, including DSA, reconnection, and many turbulent processes. The spectral index of the non-thermal particles can, in each instance, span a wide range of possibilities, as discussed below. An estimate of which mechanism is likely to be dominant can be made by comparing their relative efficiencies.

2.1.1 Reconnection

In CWB systems, particles may be accelerated at the contact discontinuity between the two winds as magnetic field lines from the two stars are forced together and reconnect (Jardine, Allen & Pollock 1996), and/or within the volume of the WCR as tangled field lines reconnect. Reconnection can occur either as a quasi-steady, or as an explosive, process. The energy released is transferred into thermal energy through direct Joule heating of the plasma, into the kinetic energy of macroscopic motions, and into accelerated particles. Unfortunately, the role of magnetic reconnection in accelerating particles is complex, not least because of the many different types of reconnection, and the intricate magnetic environment that is usually associated with reconnection. This environment can accelerate particles directly (through

strong electric fields), stochastically (i.e. through the second-order Fermi process due to high turbulence), and at the MHD shock waves which are an integral part of a reconnecting field (i.e. through DSA - see Priest & Forbes 2000, and references therein). Reconnection is usually thought to produce steep spectra i.e. $p > 2$, such as is seen in solar flares.

A rough upper limit of the power available for particle acceleration due to reconnection can be estimated as follows. If reconnection occurs as a quasi-steady process, the power released in a current sheet of area A is

$$P \approx \frac{\pi}{4 \ln R_m} \frac{B^2}{8\pi} v_A A, \quad (1)$$

where R_m is the magnetic Reynold's number, B is the magnetic field strength, and v_A is the Alfvén speed (Petschek 1964). If reconnection occurs at the contact discontinuity, the area of the current sheet, A , is approximately the area of the apex of the WCR i.e. $A \sim \pi r_O^2$, where $r_O = \eta^{1/2} D / (1 + \eta^{1/2})$ is the distance from the stagnation point of the WCR to the center of the O star, D is the separation of the stars, and the wind momentum ratio $\eta = \dot{M}_O v_O / \dot{M}_{WR} v_{WR}$ where \dot{M}_O and \dot{M}_{WR} are the mass-loss rates of the O and WR stars with terminal wind speeds of v_O and v_{WR} respectively. For our model B (see Table 1), $R_m \sim 10^{20}$, $A \sim 5 \times 10^{27} \text{ cm}^2$, $v_A \approx 6 \times 10^7 \text{ cm s}^{-1}$, and $B = 1.2 \text{ G}$, so $P \sim 3 \times 10^{32} \text{ erg s}^{-1}$. Since P is strongly dependent on B , the available power from reconnection could be considerably higher than this estimate, and may be further augmented by reconnection occurring throughout the WCR region. While we expect that only a fraction of this total power will end up in non-thermal particles, there is probably sufficient reconnection luminosity to produce the synchrotron emission observed from WR 140 ($\sim 5 \times 10^{32} \text{ erg s}^{-1}$). However, it may struggle to supply the energy in IC γ -ray emission, which is expected to be $\sim 10 \times$ greater (see Table 5).

2.1.2 Turbulent mechanisms

Particles may also be accelerated stochastically, by magnetic scattering off turbulent motions (Fermi 1949). In this mechanism, non-thermal particles either gain or lose energy depending on whether the magnetic field is moving towards or away from the particle. However, as the scattering probability is proportional to the relative velocity between the particle and the plasma, there is a slight excess of head-on scatterings and a mean increase in momentum. This process is known as the second-order Fermi mechanism, and in principle, hard power-law spectra ($p < 2$) may be obtained. The second-order Fermi mechanism is slower and less efficient than DSA (a first-order Fermi process) in our models of WR 140, since the pre-shock Alfvénic Mach number, $M_A = v\sqrt{4\pi\rho}/B \gtrsim 3$ - see Table 1. Another possible mechanism is acceleration in turbulence from resistive magnetohydrodynamical fluctuations (Nodes et al. 2004) that can produce hard power-law spectra with $p < 2$.

2.1.3 Diffusive shock acceleration

DSA is a variant of the original Fermi mechanism, in which particles are accelerated by scattering back and forth across

a shock. The key difference is that fast particles gain energy *each* time they are scattered back across the shock, until their eventual loss downstream of the shock. To a first approximation, DSA produces a power-law energy distribution of non-thermal particles (see Pittard et al. 2006, for a discussion of departures from this). The maximum power that is available to DSA is the kinetic luminosity of that part of the stellar winds which are processed through the WCR (in model B this is $\sim 10^{36}$ erg s $^{-1}$). Therefore, DSA easily meets the energy requirements for producing the synchrotron emission seen from WR 140 ($\sim 5 \times 10^{32}$ erg s $^{-1}$).

At a single, parallel shock the value of p is determined by the compression ratio of the scattering centers across the shock, r_k (e.g., Bell 1978). In the strong shock limit, the gas compression ratio $r = 4$; if $r_k \approx r$, then $p \approx 2$. However, p can be greater or smaller than this value depending on the values of r and the ratio of gas to magnetic pressure in the upstream flow, which together determine r_k (Schlickeiser 2002).

There are additional ways in which the spectral index can vary from the canonical strong shock limit of $p = 2$. For instance, when particle acceleration is efficient, the diffusion of non-thermal particles upstream of the sub-shock exerts a significant back-pressure on the pre-shock flow, causing the gas velocity to decrease prior to the sub-shock in a smooth precursor (Fig. 1). As the highest energy particles are able to diffuse further upstream from the subshock, and see the greatest velocity difference between the upstream and downstream flow, a concave curvature to the non-thermal particle energy spectrum is created. In addition, the velocity jump across the subshock in this situation is much less than in the classical shock, which results in a reduced post-shock thermal temperature. Convincing evidence for such “shock modification” is provided by analysis of observations of several young SNRs, including Tycho (Volk et al. 2002) and SN 1006 (Bamba et al. 2003; Berezhko, Ksenofontov & Völk 2003), and from direct spacecraft measurements of the Earth’s bowshock and interplanetary shocks (see references in Ellison & Cassam-Chenaï 2005). Non-thermal ions are believed to be primarily responsible for modifying shocks because they are thought to dominate the non-thermal energy density (see Sec. 2.2). Since the diffusion length of electrons is much smaller than ions for a given Lorentz factor, non-thermal electrons are confined to a region much closer to the subshock. Thus, only those electrons with momenta $\gtrsim m_p c$ (i.e. with Lorentz factors $\gtrsim 2000$) are able to diffuse far enough upstream to see the velocity difference required to obtain a spectral index $p < 2$ (assuming $p = 2$ for the unmodified shock - see Fig. 1 in Ellison, Decourchelle & Ballet 2004). In CWB systems, the synchrotron emission at GHz frequencies is from electrons with relatively low momentum. For example, at the apex of the WCR in model B of this work, electrons with $\gamma = 50$ (i.e. momentum $p = 50 m_e c \approx 0.03 m_p c$) produce synchrotron emission which peaks at $\nu = 0.29 \nu_c \approx 3.6$ GHz, where ν_c is the frequency where the synchrotron spectrum cuts off (Pacholczyk 1970). Hence, if shock modification occurs in these systems, the synchrotron emission should be characterized by $p > 2$, though if re-acceleration occurs this is not necessarily the case.

The spectral index of non-thermal particles can be modified if they pass through a sequence of shocks. In the limit

of many shocks, the spectral index approaches $p = 1$, independent of the shock strength. This process is known as “re-acceleration” (see Pope & Melrose 1994, and references therein), and if the particles suffer energy losses between the accelerating shocks, p can become even smaller (Schlickeiser 1984; Melrose & Crouch 1997). Shock modification and particle re-acceleration are not necessarily mutually exclusive.

Some previous works (Kirk & Heavens 1989; Naito & Takahara 1995) have also claimed that $p < 2$ can be obtained if the shock is oblique (i.e. when the B-field is at some angle to the shock normal), but these rely on a non-standard shock acceleration model, such as non-isotropic scattering, and we do not consider this further. Mechanisms which increase the effective Mach number of the shock may also yield $p < 2$ (e.g., Malkov et al. 2000), while $p > 2$ may be obtained if sub-diffusive cross-field transport is important (Duffy et al. 1995; Kirk et al. 1996).

2.1.4 Summary of assumed NT particle spectrum

From energy considerations, DSA and reconnection appear to be the most efficient mechanisms, with DSA likely having the edge (see also Bednarek 2005). Therefore, for the remainder of this work we assume that the non-thermal particles (electrons and ions) are created by DSA at the global shocks bounding the WCR and have power-law energy distributions. We further assume that the downstream magnetic field is highly tangled. While we do not model the actual acceleration process itself, this is consistent with the Bohm limit where the magnetic fluctuations are of the same strength as the background field i.e. $\delta B/B \sim 1$. The strong cross-field diffusion which results in this limit allows efficient injection at quasi-perpendicular shocks.

The diffusion length scale of accelerating particles is given by $l_{\text{diff}} = \kappa/v_{\text{shk}}$, where v_{shk} is the shock speed, $\kappa = \lambda v/3$ is the spatial diffusion coefficient, $\lambda \approx 3r_g$ is the mean-free-path, and $r_g = \gamma mc^2/qB$ is the gyroradius of particles with Lorentz factor γ , mass m , and charge q in a magnetic field B . The acceleration of non-thermal electrons at the shocks is not affected by the flow geometry of the downstream plasma, as the diffusion lengthscale is only a small fraction of the width of the WCR (e.g., $l_{\text{diff}} \sim 10^{10}$ cm for electrons with $\gamma = 10^5$ at the shock apex of model B, whereas the distance between the global shocks and the contact discontinuity is $\approx 2 \times 10^{13}$ cm). Therefore, the geometry of the post-shock flow will have no impact on our calculation of the synchrotron and IC emission, or our finding that the electron spectrum has $p < 2$. The flow geometry may become important for non-thermal ions, but for protons and He nuclei this is only likely to be the case for $\gamma \gtrsim 10^4$. Detailed work outside the scope of this paper is required to examine the effect of the flow geometry on our predictions of the high energy emission from the decay of neutral pions.

We do not consider the inverse-Compton (IC) cascade of secondary electrons and positrons that occur when the optical depth of γ -rays to pair-production in a stellar radiation field is high and when IC scattering is efficient, though in WR 140 the secondary γ -rays produced in the cascade and which subsequently escape the system may be comparable to the observed flux of primary γ -rays above GeV energies for the orbital phase considered in this work (cf. Bednarek 2006). The non-thermal electrons formed by hadronic colli-

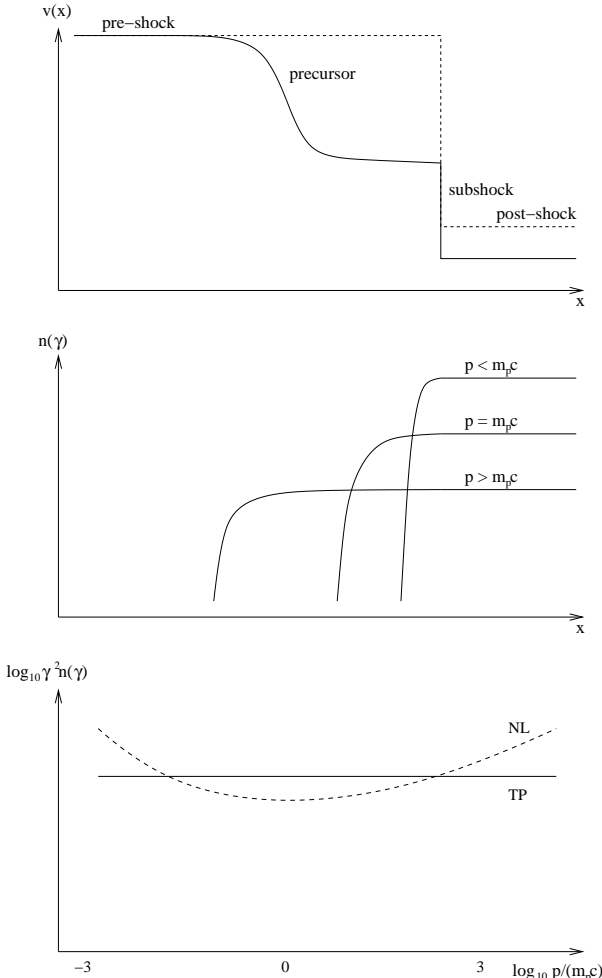


Figure 1. Top: Schematic structure of a strong hydrodynamic shock. If DSA places a negligible amount of energy into accelerated particles, an ordinary discontinuous classical shock occurs (dashed line). In this case the undisturbed pre-shock flow is separated from the post-shock flow by a discontinuity known as a subshock across which the flow velocity decreases, and the density and pressure increase. The scale length of the subshock, l_s , is determined by microphysical dissipation processes that result in gas heating. In contrast, when particle acceleration is efficient, the diffusion of non-thermal particles upstream of the subshock exerts a back-pressure on the pre-shock flow, causing the gas velocity to decrease prior to the subshock in a smooth precursor (solid line). The scale length of the precursor, l_d ($\gg l_s$), is approximately the diffusion length of the highest energy ions. Middle: The spatial distribution of the number density of non-thermal particles as a function of energy in the modified shock. The highest energy particles are able to diffuse further upstream from the subshock, and see the greatest velocity difference between the upstream and downstream flow. Non-thermal particles in the precursor are typically scattered back across the subshock, and either undergo further acceleration, or escape downstream. Bottom: The non-thermal particle energy spectrum multiplied by γ^2 to emphasize the spectral curvature of the non-linear (i.e. efficient particle acceleration) case. When DSA places relatively little energy into accelerated particles the standard test particle spectrum is obtained, as shown here for $p = 2$ (solid). In contrast, the modified shock produced when DSA is efficient leads to a concave curvature in the non-thermal particle energy spectrum (dashed - see Ellison, Decourchelle & Ballet 2004, and references therein).

sions, and the knock-on electrons formed when non-thermal nuclei collide with thermal (atomic and free) electrons, are also ignored in this work, though the emission resulting from these processes is not expected to be dominant (see also Mastichiadis 1996; Baring et al. 1999; Berrington & Dermer 2003). We also ignore an additional (though likely small) contribution to the non-thermal radio emission from particles accelerated at wind-embedded shocks caused by the line-deshadowing instability in radiatively driven winds, since in WR 140 the non-thermal emission is clearly related to binarity. We set p as a free parameter for the particle distribution immediately downstream of the shocks, with the assumption that it is spatially invariant along the face of the shocks, and identical for electrons and ions. For the ions p does not change in the post-shock flow, but as the non-thermal electrons advect downstream IC cooling modifies their energy distribution, and in this case p is dependent on both their spatial position and γ (Pittard et al. 2006). For instance, in model B, electrons accelerated at the WR shock on the line of centers between the stars cool to $\gamma \lesssim 100$ within a time of $\approx 6.3 \times 10^4$ s, during which they are advected a distance of $\approx 4.7 \times 10^{12}$ cm (0.015 D) downstream (assuming that the speed of the post-shock flow is 0.25 v_∞ in this region of the WCR). Electrons accelerated at a point on the WR and O shocks which is a distance D from the O star cool to $\gamma \lesssim 1000$ within a time of $\approx 2 \times 10^5$ s. During this time they are advected a distance of 5.9×10^{13} cm (0.19 D) downstream (assuming a post-shock flow speed close to the terminal wind speeds).

2.2 Normalization

2.2.1 The non-thermal particle spectrum

Since the population of non-thermal particles is not determined from first principles in our models, the non-thermal electron energy density, $U_{\text{rel,e}}$, is assumed to be proportional to the thermal particle internal energy density, U_{th} i.e. $U_{\text{rel,e}} = \zeta_{\text{rel,e}} U_{\text{th}}$. Also, it is assumed that shock obliquity does not influence the normalization of the non-thermal electron energy density. However, we note that in general, the higher the obliquity, the lower the injection efficiency (although particles are actually accelerated more rapidly as a result of shock drift along the surface and slower diffusion in the shock normal direction - see, e.g., Ellison, Baring & Jones 1995, 1996; Ellison, Jones & Baring 1999). In wide binaries, such as WR 140, the shocks near the head of the WCR should, in principle, be highly oblique. Yet this picture is further complicated if the level of magnetic turbulence is at the Bohm limit, since then the shock does not have a well-defined obliquity, and strong cross-field diffusion results in efficient injection (see Fig. 6 in Ellison, Baring & Jones 1995). Such concerns are beyond the scope of the present work.

To obtain an estimate of the γ -ray flux from the decay of neutral pions, the energy density of relativistic ions must be specified. Similar to the non-thermal electrons, it is assumed that $U_{\text{rel,i}} = \zeta_{\text{rel,i}} U_{\text{th}}$. Fits to the radio data are only sensitive to $\zeta_{\text{rel,e}}$ and constraining $\zeta_{\text{rel,i}}$ requires unambiguous detection of the emission from neutral pion-decay, which has not been attained for CWB systems. Moreover, the relative injection efficiency of electrons and ions is not

known, while the value of $\zeta_{\text{rel},i}/\zeta_{\text{rel},e}$ also depends on the spectral index p (Schlickeiser 2002). Having said this, it is reasonably certain that DSA transfers considerably less energy into non-thermal electrons than into non-thermal ions (e.g., Baring et al. 1999), while the relative difficulty of accelerating electrons is also consistent with the well established value for the ratio of proton to electron energy densities for Galactic cosmic rays of ~ 100 (Longair 1994). In this work we somewhat arbitrarily assume that $\zeta_{\text{rel},i} = 100\zeta_{\text{rel},e}$, unless otherwise noted, though the actual ratio in WR 140 could differ significantly. As a result, our predictions of the γ -ray flux from neutral pion decay and neutrino flux from charged pion decay are highly uncertain. However, hard upper limits for these fluxes can be obtained due to the requirement that the total power put into non-thermal particles must be less than the available kinetic power in the WCR i.e. $\zeta_{\text{rel},e} + \zeta_{\text{rel},i} \lesssim 1$.

As non-thermal particles flow downstream, they are subject to adiabatic losses. This is achieved in an approximate fashion in this work through the assumption that $U_{\text{rel},e}$ and $U_{\text{rel},i}$ are proportional to U_{th} . In reality the adiabatic indices for thermal and relativistic plasma differ, and adiabatic expansion also reduces the Lorentz factor of the particles. While neither of these effects is treated properly in our model, the specific parameterization we have chosen will not lead to significant errors in the resulting non-thermal radio emission. This is because IC cooling is so rapid for high energy electrons that synchrotron emission above ~ 1 GHz is largely confined to a thin region near the shocks, where the effects of adiabatic expansion of the flow are minimal. Likewise, the radiation from pion decay is concentrated near the apex of the WCR.

2.2.2 The magnetic field

If the field is frozen into the post-shock plasma of density ρ , one would anticipate $B \propto \rho$ ($U_B \propto \rho^2$), but amplification of the magnetic field by the accelerated particles (e.g., Bell 2004) and/or reconnection complicates this simple scaling. This also implies that it is not necessarily straightforward to determine the B-field in the WCR from assumptions about the strength of the surface magnetic field at each star. Indirect evidence for amplification has recently been obtained in several SNRs (e.g., Berezhko, Ksenofontov & Völk 2003; Berezhko & Völk 2004; Ellison & Cassam-Chenä 2005). Instead, for convenience, we have assumed that the magnetic energy density is proportional to the thermal particle energy density i.e. $U_B = \zeta_B U_{\text{th}}$. This choice is equivalent to some amplification in the downstream flow, but we have verified that there is little difference in the shape of the synchrotron spectrum between these two methods. Compared to other work where the B-field is assumed to be spatially invariant, this approximation at least has the benefit that the B-field declines away from the symmetry axis. Undoubtedly, a better description for the B-field will be obtained in future MHD models of the WCR. Our final assumption is that the post-shock B-field is highly tangled so that the synchrotron emission is isotropic.

2.2.3 Limits on ζ_B and $\zeta_{\text{rel},e}$

When modelling the radio emission from specific systems, ζ_B and $\zeta_{\text{rel},e}$ are chosen to best match the observed radio emission. As ζ_B decreases, the value of $\zeta_{\text{rel},e}$ has to increase to reproduce an observed radio flux. A lower limit on ζ_B can be obtained from the fact that the Razin turnover frequency, ν_R , increases with declining ζ_B ($\nu_R \approx 20n_e/B$, where n_e is the electron number density and the magnetic field, $B = \sqrt{8\pi U_B}$), or because the value of $\zeta_{\text{rel},e}$ required to match an observed flux exceeds the available power for particle acceleration in the WCR. An upper limit on ζ_B is obtained from the necessary conditions for particle acceleration (see Eichler & Usov 1993). Since there is currently little guidance for the ratio of $\zeta_B/\zeta_{\text{rel},e}$ in CWB systems, we consider this to be a free parameter in our models, subject to the above constraints.

2.3 Maximum energy of non-thermal particles

The maximum value of γ for electrons is obtained by balancing the rate of energy increase from DSA to the rate of energy loss by IC cooling (e.g., see Eqs. 4 and 7 in Pittard et al. 2006). This is spatially dependent due to the geometric dilution of both the stellar radiation and magnetic fields, and also dependent on orbital phase for binaries with eccentric orbits like WR 140. An evaluation of these equations at the points where the shocks intersect the line of centers through the stars reveals that $\gamma_{\text{max}} \sim 10^5$ at orbital phase 0.837 for sensible values of B . Most of the wind power passing into the WCR occurs within an off-axis distance of $\sim 2r_0$ from the line of centers (Pittard & Stevens 2002), and one expects that most of the energy transfer into non-thermal particles must occur within this volume too. The value of γ_{max} evaluated at a position on the shock front at the extremity of this region is only 25 per cent higher than on the line of centers if the magnetic field strength is assumed to decline as $1/r$ and if there is no dependence on the shock obliquity (as already mentioned, this is not well defined if the level of magnetic turbulence is at the Bohm limit). Therefore, for simplicity, throughout this work it is assumed that $\gamma_{\text{max}}(\text{electrons}) = 10^5$ along the entire shock fronts.

While the above evaluation was for the Thomson limit, at such energies IC losses occur in the Klein-Nishina regime, and the spectral distribution as well as the cut-off energy will change. However, in the calculations in this paper, IC cooling is so rapid near the apex of the WCR that the downstream population of non-thermal electrons in this region is essentially independent of whether Thomson or Klein-Nishina cross-sections are used. Thus, the IC emission and our predictions for the γ -ray fluxes are essentially identical too, with the exception that the high energy cutoff is sensitive (by a factor of order 2) to such details.

The maximum non-thermal ion energy is set by balancing the timescale of their acceleration to their advection timescale out of the system. Following Bednarek (2005)¹,

$$\gamma_{\text{max}}(\text{ions}) = \frac{3ZeBrov}{c^3 Am_p} \quad (2)$$

¹ In Eq. 3 of Bednarek (2005) the denominator should have a factor c^3 as shown here in Eq. 2.

where Ze and Amp are the charge and mass of the ion, and B and v are the pre-shock magnetic field and wind speed. For wide binaries where the pre-shock magnetic field declines as $1/r$, $\gamma_{\max}(\text{ions})$ is expected to be independent of D .

For the models considered in this paper, $\gamma_{\max}(\text{ions}) \sim 10^5$, so for convenience, we set $\gamma_{\max} = 10^5$ for both the electron and ion distributions in the remainder of this work. The predicted γ -ray flux is, of course, sensitive to the value of γ_{\max} chosen for both the electrons and ions. In addition, $\gamma_{\min} = 1$ is assumed.

2.4 Composition of non-thermal nuclei

In the simplest test-particle calculations of DSA i.e. with no feedback, all particles accelerated in a given shock will have identical power-law spectral shapes in momentum, regardless of their charge, and the non-thermal particle composition reflects the composition of thermal particles. However, in non-linear models, the spectral shape and injection and acceleration efficiencies are dependent on the ionic species. Ions with large mass-to-charge (A/Q) ratios diffuse further upstream than protons of the same energy per nucleon (provided that both are non-relativistic), and are accelerated more efficiently and obtain a flatter spectrum because they “see” a larger velocity difference and are more easily injected to suprathermal energies. Among the volatile elements, observational support comes from Galactic cosmic rays, which show an enhancement of heavier elements relative to lighter ones (Meyer, Drury & Ellison 1997). A general enhancement of the refractory elements relative to the volatile ones is also apparent from the Galactic cosmic ray composition (Meyer, Drury & Ellison 1997). This has been explained by acceleration of dust grains (which can have huge mass-to-charge ratios of $\sim 10^4 - 10^8$), followed by the sputtering of atoms from these grains. However, the harsh UV radiation fields in CWB systems makes it unlikely that dust grains can form near the head of the WCR, so an enhancement of refractory elements is not expected. Several CWB systems, including WR 140, show observational signatures of either episodic or continuous dust formation (e.g., Williams 1996; Tuthill et al. 1999; Marchenko et al. 2002), though in all cases the dust is thought to form well downstream of the apex of the WCR. Observations have further revealed that the relative abundance of heavy ions increases with energy (see Bykov & Toptygin 2001; Hillas 2005). This is supported by the results from non-linear models where variation with shock speed and Mach number is also seen (Ellison, Drury & Meyer 1997). It is also possible that shock obliquity may influence the non-thermal particle composition.

High energy heavy nuclei may also lose nucleons due to collisions with stellar photons i.e. by photo-disintegration. This occurs if the photon energy in the reference frame of the nuclei, $E_\gamma = 3k_B T \gamma (1 + \cos \theta)$, exceeds ~ 2 MeV (Bednarek 2005). Here T is the temperature of the radiation field. In WR 140, this process applies to nuclei with $\gamma \gtrsim 8.5 \times 10^4$, and is only likely to affect a small part of the top end of the non-thermal particle distribution. In addition, an estimate of the ratio of the characteristic photo-disintegration timescale to the acceleration and advection timescales reveals that photo-disintegration is not efficient for particles with $\gamma \lesssim 10^5$ in WR 140 at the orbital phase considered in this work. The

fragmentation of high energy nuclei through collisions with thermal ions is likewise negligible.

Given the uncertainties discussed earlier, we adopt the following simplifications: i) identical spectra for all non-thermal particles, ii) identical composition to that of the thermal particles, iii) no dependence on the shock obliquity.

3 NON-THERMAL X-RAY AND γ -RAY EMISSION AND ABSORPTION

The presence of non-thermal electrons and ions should give rise to X-ray and γ -ray emission from several separate mechanisms, including IC scattering, relativistic bremsstrahlung, and pion decay (the non-thermal electrons are not energetic enough to produce synchrotron X-ray emission). While definitive evidence for non-thermal X-ray and γ -ray emission from CWBs does not yet exist, many of the yet unidentified EGRET sources appear correlated with populations of massive stars (Romero, Benaglia & Torres 1999), and some systems appear to show a power-law tail extending to higher energies than the thermal X-ray emission (Viotti et al. 2004; De Becker et al. 2004b). A critical question is whether the non-thermal X-ray and γ -ray fluxes from CWB systems are sufficiently high to be detected with instruments onboard current observatories, and instruments on observatories that will be operational in the near future.

Previous predictions of the IC emission have usually been based on the fact that the ratio of the luminosity from IC scattering to the synchrotron luminosity is equal to the ratio of the photon energy density, U_{ph} , to the magnetic field energy density, U_B :

$$\frac{L_{\text{ic}}}{L_{\text{sync}}} = \frac{U_{\text{ph}}}{U_B}. \quad (3)$$

Typically, the ratio of U_{ph}/U_B is evaluated only at the stagnation point, whereas in reality the emission is generated throughout the WCR, with U_{ph}/U_B varying spatially. In addition, L_{sync} is usually set to the *observed* synchrotron luminosity, whereas free-free absorption by the extended wind envelopes can be significant (see, e.g., Pittard et al. 2006). In such cases the intrinsic synchrotron luminosity, and consequently the non-thermal X-ray and γ -ray luminosity, will be underestimated if radio data, particularly at lower frequencies, are used without regard to free-free absorption (cf. Figs. 5, 14 and 15). Furthermore, the predictive power of Eq. 3 is greatly undermined by the fact that the magnetic field strength in the WCR is generally not known with any certainty. Since $U_B \propto B^2$, small changes in the estimated value of the magnetic field strength, B , can lead to large changes in L_{ic} (see Fig. 3 in Benaglia & Romero 2003).

To obtain a more robust estimate of the IC emission from CWB systems, the population and spatial distribution of non-thermal electrons must be determined directly. This information can, in principle, be acquired from model fits to radio data, since the IC emission arises from the same non-thermal electrons responsible for the synchrotron radio emission. As already noted, an improved theoretical basis for the modelling of the radio emission from such systems was developed by Dougherty et al. (2003) and Pittard et al. (2006), and we use this as the foundation for our calculations of the non-thermal X-ray and γ -ray emission. Key benefits

over previous work include a more realistic description of the geometry of the WCR, the evolution of the energy distribution of the non-thermal electrons as they advect downstream from their acceleration site, and absorption of high energy photons by pair production in the stellar radiation fields. Our predictions for the expected γ -ray emission are based on model fits to the available radio and X-ray data, which allow us to constrain the range of free parameters and build in a degree of consistency for our estimates.

3.1 IC emission

IC cooling is a major energy loss mechanism for non-thermal electrons in CWB systems, and the non-thermal X-ray and γ -ray luminosity should exceed the synchrotron radio luminosity by several orders of magnitude. In the Thomson regime, the average energy of a photon after isotropic IC scattering is (Blumenthal & Gould 1970)

$$h\nu_{\text{IC}} \sim \frac{4}{3}\gamma^2 h\nu_* . \quad (4)$$

Since the average photon energy of an early-type star, $h\nu_* \sim 10$ eV, Lorentz factors of order $10 - 10^4$ are sufficient to produce IC X-ray and γ -ray radiation up to GeV energies. The resulting emission has a spectral shape which is identical to the intrinsic synchrotron emission at radio frequencies. For our calculations, we assume that the scattering is isotropic and takes place in the Thomson limit. While a more thorough treatment would take account of Klein-Nishina effects, which are important at high energies, recent work has shown that the resulting change to the non-thermal electron energy distribution is rather small when the stellar separation is $\gtrsim 2 \times 10^{14}$ cm (Reimer, Pohl & Reimer 2006). This condition is satisfied in WR 140 between orbital phases $\phi = 0.1 - 0.9$, and also in wider binaries like WR 146 and WR 147.

Consideration should also be given to the anisotropic nature of the IC process, where the emitted power is dependent on the scattering angle. However, if the O star is in front of the WR star (which is the case for WR 140 at $\phi = 0.837$ - see Sec. 4), the variation in the resulting emission is less than a factor of 2.5 (Reimer, Pohl & Reimer 2006). In Sec. 4.4.1, we show that the other uncertainties affecting the IC emission, such as the value of ζ_e determined from fitting the radio data, are at least comparable in magnitude, so we leave this issue to future work.

3.2 Relativistic Bremsstrahlung

Bremsstrahlung radiation is produced when a charged particle is accelerated in the Coulomb field of another charged particle. It is possible to obtain emission at γ -ray energies if one of the particles is relativistic, since photons of comparable energy to that of the emitting particle can be produced. Inverse bremsstrahlung, produced by collisions between high energy ions and thermal electrons, is an insignificant contribution to the total emission unless the ratio of the energy density of non-thermal ions to electrons is very high. Therefore, we concentrate on emission produced by collisions between non-thermal electrons and thermal electrons and ions. A more detailed discussion can be found in Baring et al. (1999).

The rate of photon production in the energy interval between ϵ_γ and $\epsilon_\gamma + d\epsilon_\gamma$ by an electron of kinetic energy E_e is

$$\frac{dn_\gamma(E_e, \epsilon_\gamma)}{dt} = v_e \left[n_e \sigma_{ee}(E_e, \epsilon_\gamma) + \sum_i n_i Z_i^2 \sigma_{ep}(E_e, \epsilon_\gamma) \right], \quad (5)$$

where ϵ_γ is the photon energy in units of $m_e c^2$, v_e is the relative velocity of the colliding particles, n_i and n_e are the number density of ions and electrons respectively, and Z_i is the charge of the ion. The electron-proton cross section, σ_{ep} , is the Bethe-Heitler cross section evaluated in the Born approximation. We determine σ_{ep} for any electron energy, relativistic or non-relativistic, using equation 3BN in Koch & Motz (1959), and omit the Coulomb corrections at low energies. The cross section for electron collisions with fully ionized ions has a Z^2 charge dependence, accounting for the factor in Eq. 5. For the electron-electron cross section, σ_{ee} , the approach noted in Baring et al. (1999) is followed.

For $\gamma_e \gg 1$ and $\epsilon_\gamma \gg 1$, the cross sections depend only on the particle's charge and not its mass, so $\sigma_{ep} = \sigma_{ee}$. The ratio of the electron-electron to electron-ion contributions is then simply

$$\frac{n_e}{\sum_i Z_i^2 n_i}. \quad (6)$$

For material with solar abundances this ratio is ≈ 0.86 , while in the shocked WR wind of WR 140 it is ≈ 0.47 (see Sec. 4). At high energies, the bremsstrahlung spectrum (in units of $\text{photons s}^{-1} \text{cm}^{-2}$) has a spectral index which reflects that of the non-thermal particles i.e. p .

3.3 π^0 decay

High energy hadronic collisions can create neutral pions which subsequently decay into two γ -ray photons, e.g., $p + p \rightarrow \pi^0 + X, \pi^0 \rightarrow \gamma + \gamma$. The final stage has a branching ratio of $\approx 98.8\%$ (the decay $\pi^0 \rightarrow \gamma + e^+ + e^-$ accounts for the other 1.2%). The pion decay process yields information on the population of non-thermal nucleons, in contrast to the IC and bremsstrahlung processes where the emission is dependent on the population of non-thermal electrons.

The cross-section for hadronic collisions depends on the ionic species involved, so we first consider the π^0 emissivity from proton-proton collisions. The production rate for neutral pions of energy E_π per thermal proton can be easily evaluated using a δ -functional approximation for the differential cross-section (Aharonian & Atoyan 1996):

$$q_\pi(E_\pi) = \int \delta(E_\pi - f_\pi E_k) \sigma_{pp2}(E) J(E) dE, \quad (7)$$

where E_k is the kinetic energy of the non-thermal protons, f_π is the fraction of the kinetic energy of the non-thermal proton which is transferred to the π^0 meson, σ_{pp2} is the total inelastic cross section (Aharonian & Atoyan 1996), and $J(E)$ is the flux of non-thermal protons of total energy E ($\text{protons s}^{-1} \text{cm}^{-2} \text{GeV}^{-1}$). Here, only the contribution to the γ -ray emission from the neutral pion is considered. After the interaction the non-thermal proton keeps approximately half of its energy, while the other half goes to pions. On average the neutral pion gets approximately one third of this energy, or approximately one sixth of the energy of the

non-thermal proton, so $f_\pi = 0.17$. Thus, Eq. 7 becomes (pions $\text{s}^{-1} \text{GeV}^{-1} \text{H}^{-1}$):

$$q_\pi(E_\pi) = \frac{1}{f_\pi} \sigma_{\text{pp2}}(E) J(E). \quad (8)$$

The γ -ray emissivity (photons $\text{s}^{-1} \text{GeV}^{-1} \text{H}^{-1}$) is then

$$q_\gamma(E_\gamma) = 2 \int_{E_{\min}}^{\infty} \frac{q_\pi(E_\pi)}{\sqrt{E_\pi^2 - m_\pi^2 c^4}} dE_\pi, \quad (9)$$

where $E_{\min} = E_\gamma + m_\pi^2 c^4 / 4E_\gamma$ and m_π is the mass of the neutral pion (134.9766 MeV/c²).

In CWB systems, we must account for the composition of non-thermal and thermal ions. For collisions involving two nuclei with atomic weights A_1 and A_2 , the cross section is (Orth & Buffington 1976)

$$\sigma \sim (A_1^{3/8} + A_2^{3/8} - 1)^2 \sigma_{\text{pp2}}. \quad (10)$$

This prescription is appropriate for proton-helium interactions, but its validity for heavy nuclei, such as Fe, is unclear. It is adopted here since its potential inaccuracy is small compared to the other uncertainties and assumptions in this work. In the case of WR stars, such as WR 140, the wind contains little or no hydrogen, and the cross-section for pion decay is best calculated relative to the He-He cross section $\sigma_{\alpha\alpha} = 5.6\sigma_{\text{pp2}}$.

Considering only protons and Helium nuclei, an enhancement to the pion production rate in Eq. 8 of 1.61 is obtained for material of solar composition. Greater enhancements are obtained for the nuclear processed material in WR winds. For example, if collisions involving He, C, O and Ne are considered for the WC7 wind abundances in WR 140 (see Sec. 4.2.1), then $\sigma \sim 1.4\sigma_{\alpha\alpha} \sim 7.8\sigma_{\text{pp2}}$.

3.4 γ -ray absorption

γ -rays above a suitable threshold energy may create electron-positron pairs via interaction with a lower energy photon or with charged nuclei. While the latter process has an insignificant optical depth in CWB systems, in contrast the high stellar radiation energy density may be a significant source of opacity to high energy γ -rays. The probability of absorption depends on the cosine of the angle between the directions of the two photons, μ . For a high energy photon of energy E_γ interacting with a stellar photon of energy ϵ , the optical depth is given by

$$\frac{d\tau}{dr} = \int \sigma(\chi) (1 - \mu) n(\epsilon, \mu, r) d\epsilon d\mu, \quad (11)$$

where $\chi = \sqrt{E_\gamma \epsilon (1 - \mu) / 2}$ is the centre-of-momentum frame energy² scaled by $m_e c^2$,

$$\sigma(\chi) = \frac{\pi r_e^2}{\chi^6} \left[(2\chi^4 + 2\chi^2 - 1) \ln(\chi + \sqrt{\chi^2 - 1}) - \chi(1 + \chi^2) \sqrt{\chi^2 - 1} \right], \quad (12)$$

where $r_e = e^2 / m_e c^2$, and $n(\epsilon, \mu, r)$ is the number density of stellar photons. The threshold for pair production, and thus for absorption, is $\chi \geq 1$.

² The equation for χ contains a typo in Baring & Harding (1997).

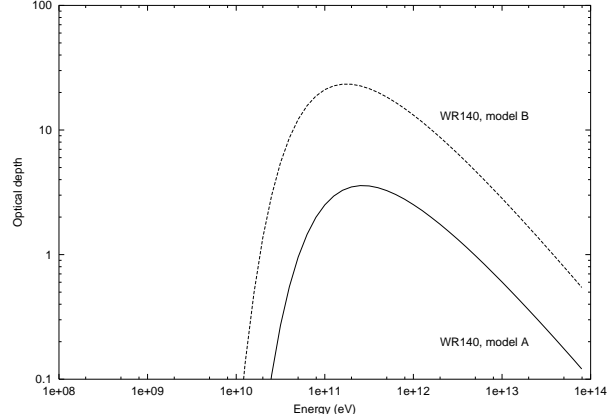


Figure 2. The optical depth from two-photon pair production as a function of the non-thermal photon energy for a single line-of-sight from the stagnation point of the WCR in WR 140. The shape of the curves reflects the Planck distribution for the stellar photons ($T = 45,000$ K). We show calculations at $\phi = 0.837$ for models A and B (see Sec. 4). In each case, only the photons from the O star are considered. The energy of peak absorption is a function of the viewing angle, θ , and increases as θ decreases.

In wide CWBs it can be assumed that the stars are point-like, and that the stellar photons stream radially away from each star. This allows the $(1 - \mu)$ term to be taken out of the integral in Eq. 11. The optical depth as a function of non-thermal photon energy from the stagnation point to an observer for two models of WR 140 is shown in Fig. 2. Table 1 summarizes some key parameters of these models.

Of the two models shown in Fig. 2, both the shock apex and the line of sight from the apex are closer to the O star in model B. The greatest opacity occurs at ~ 100 GeV, where optical depths as high as ~ 25 (model B) may be reached. At lower and higher energies the optical depth decreases, and optical depth unity occurs at approximately 50 GeV and 5 TeV for model A, and at approximately 20 GeV and 40 TeV for model B. In practice, the effective optical depth is likely to be somewhat smaller due to the spatial extension of the emission region. More accurate calculations using radiative transfer along multiple sight lines are presented in Sec. 4.4. The CWB system WR 146, which has a wider stellar separation, is expected to have a maximum optical depth to pair-production of ~ 1 . In WR 147, which is wider still, the attenuation is negligible. Similar conclusions have also been noted by Reimer, Pohl & Reimer (2006).

4 NON-THERMAL EMISSION MODELS OF WR 140

In this section we apply our model to WR 140 (HD 193793), the archetype of long-period CWB systems. WR 140 consists of a WC7 star and an O4-5 star in a highly elliptical orbit ($e \approx 0.88$), and is well known for the dramatic variations in its emission from near-IR to radio wavelengths (Williams et al. 1990; White & Becker 1995), and also at X-ray energies during its 7.9-year orbit (Zhekov & Skinner 2000; Pollock, Corcoran & Stevens 2002; Pollock et al. 2005). The variability appears to be

linked to the WCR, which experiences significant changes as the stellar separation varies between ~ 2 AU at periastron and ~ 30 AU at apastron. The observed radio emission increases by up to two orders of magnitude between periastron and a frequency-dependent peak between orbital phases 0.65 to 0.85, followed by a steep decline. The decline of the radio emission prior to periastron is consistent with the extinction suffered by the X-ray emission at these orbital phases. The X-ray lightcurve does not follow the expected $1/D$ variation for an adiabatic WCR (Pollock, Corcoran & Stevens 2002), which may indicate that the WCR becomes radiative near periastron (Varricatt, Williams & Ashok 2004). It is also possible that this discrepancy is caused by a substantial amount of the available energy in the wind-wind collision being placed into non-thermal particles, with the efficiency varying as a function of phase, though we believe this scenario should be considered as less likely.

WR 140 is also notable for its possible association with an unidentified EGRET source, lying on the outskirts of the positional error box of 3EG J2022+4317 (Romero, Benaglia & Torres 1999). The error box has a radius of $\approx 0.7^\circ$, but WR 140 is the only known high-energy source in the vicinity. 3EG J2022+4317 has a flux of $(24.7 \pm 5.2) \times 10^{-8}$ photons $\text{s}^{-1} \text{cm}^{-2}$, and a photon spectral index $\Gamma = 2.31 \pm 0.19$ (where $N(E) \propto E^{-\Gamma}$) (Hartman et al. 1999). The variability of 3EG J2022+4317 is discussed in some detail by Benaglia & Romero (2003). Since it was only detected in 3 out of 12 observing periods (at approximate orbital phases 0.97, 1.00, and 1.16), the upper limits of the remaining observations may hide real variability.

It has been suggested previously that better agreement may be obtained between observed and modelled radio lightcurves if the wind of the WR star is disc-like (White & Becker 1995), but a specific (and unusual) orientation is required for consistency with polarization measurements (see Marchenko et al. 2003, and discussion therein), and there is no evidence for such a disk in X-ray observations (Pollock, Corcoran & Stevens 2002). In the following, it is assumed that the undisturbed wind is isotropic.

4.1 Details of the model

Our calculations of the observed thermal and non-thermal emission from CWB systems are based on the density and temperature distribution obtained from 2D hydrodynamical simulations of the stellar winds and their collision (see Dougherty et al. 2003; Pittard et al. 2006). At radio frequencies, both the stellar winds and the WCR contribute thermal emission and absorption. The free-free emission and absorption coefficients are determined from the local temperature and density values on the hydrodynamic grid, and clumping is accounted for (see Sec. 4.2.4). The non-thermal emission is modelled after specifying the population and spatial distribution of non-thermal particles, as noted in Sec. 2. Additional details relating to the hydrodynamical code, and the method and assumptions used to obtain the various emission and absorption coefficients in each cell, can be found in Pittard et al. (2006) and references therein.

The assumption of axisymmetry in our 2D models is good until orbital phases of ~ 0.97 , as the orbital eccentricity is so high. Since radiative braking (Gayley, Owocki & Cranmer 1997) or inhibition

(Stevens & Pollock 1994) is not expected to be important, the wind speeds are assumed to be constant. The calculations are performed on a grid with 1600×800 cells, which spans the range $0 \leq r \leq 4 \times 10^{15} \text{ cm}$, $-4 \times 10^{15} \leq z \leq 4 \times 10^{15} \text{ cm}$, and is large enough to capture the vast majority of the radio and X-ray emission from the WCR, though inevitably the models underestimate the radio flux at the lowest frequencies considered. The line of sight into the system is specified by the angle θ , which is measured from the line perpendicular to the line of centers of the two stars: $\theta = +90^\circ$ corresponds to the O star in front of the WR star, $\theta = 0^\circ$ corresponds to quadrature, and $\theta = -90^\circ$ corresponds to the WR star in front of the O star.

4.2 Parameters of WR 140

Recent high-resolution VLBA observations at 8.4 GHz between orbital phase 0.7 and 0.9 have provided important new constraints to models of WR 140 (Dougherty et al. 2005). An arc of emission is observed, resembling the bow-shaped morphology expected for the WCR, and rotates as the orbit progresses. This rotation allows derivation of the orbit inclination and semi-major axis, leading to a geometric distance determination (1.85 ± 0.16 kpc) that is independent of stellar parameters. This distance is greater than previously thought, and implies the O star is a supergiant. Therefore, we adopt $\log(L_{\text{bol}}/L_\odot) = 6.18$ and $v_\infty = 3100 \text{ km s}^{-1}$ for the O4-5I primary, and $\log(L_{\text{bol}}/L_\odot) = 5.5$ and $v_\infty = 2860 \text{ km s}^{-1}$ for the WC7 secondary (Dougherty et al. 2005). These luminosities are higher than average for the spectral types. Herrero, Puls & Najarro (2002) and Repolust et al. (2004) suggest a typical value of 5.7-5.9 for an O4-5 supergiant, while the mean luminosity for WC7 stars is about 0.4 dex lower (although the scatter in the absolute magnitude of WC7's is ~ 1 magnitude). Therefore, there may be some scope for lowering the adopted luminosities.

Dougherty et al. (2005) used the models of Zhekov & Skinner (2000) of the observed thermal X-ray luminosity to derive a mass-loss rate for the WR star of $4.3 \times 10^{-5} M_\odot \text{ yr}^{-1}$. However, there are several complicating factors, such as the inadequate constraints on the composition of the WC7 wind and on the wind momentum ratio, η . As η increases, the opening angle of the WCR increases, and a greater fraction of the WC7 wind is shocked, resulting in an increase in the X-ray luminosity if the mass-loss rate of the WR star is unchanged. There is also the possibility of some degree of shock modification. These issues are explored in the following sub-sections, leading to improved estimates of the mass-loss rates and η in WR 140.

4.2.1 WR wind composition

The thermal X-ray emission is largely from the shocked WR star wind (Pittard & Stevens 2002). Hence, it is particularly sensitive to the abundance of He and C since the free electrons are largely stripped from these elements. For a pure He and C wind, the continuum flux scales as $(2^2 + (\text{C/He})6^2)$, where C/He is the ratio of abundance by number of C and He (Pollock et al. 2005). Unfortunately, the mass fraction of

Table 1. Some key parameters for our models of WR 140 at $\phi = 0.837$ (Sec. 4). D is the binary separation, η is the wind momentum ratio, r_O is the distance of the stagnation point of the WCR from the O star in units of the stellar separation D , and d is the distance of the system. U_{th} , U_B , U_{ph} , n_e , and B are all evaluated at the stagnation point, while the pre-shock Alfvénic Mach number, M_A , is evaluated immediately upstream of the WR shock on the line of centers, assuming that at this point the shock is highly perpendicularly and that the B-field is reduced by a factor of 4 from its post-shock value. θ is the angle of the line of sight into the system. Two values are given for n_e - these are for the WR and O star side of the contact discontinuity respectively.

Parameter	Model A	Model B
D (10^{14} cm)	3.13	
$\log(L_{\text{O,bol}}/L_{\odot})$	6.18	
$\log(L_{\text{WR,bol}}/L_{\odot})$	5.5	
d (kpc)	1.85	
η	0.22	0.02
r_O	0.32	0.124
$\zeta_{\text{rel,e}}$	1.38×10^{-3}	5.36×10^{-3}
ζ_B	0.05	0.05
U_{th} (erg cm $^{-3}$)	0.78	1.2
U_B (erg cm $^{-3}$)	0.04	0.06
U_{ph} (erg cm $^{-3}$)	1.6	10.3
n_e (WR) (cm $^{-3}$)	3.7×10^6	6.0×10^6
n_e (OB) (cm $^{-3}$)	1.3×10^7	2.0×10^7
B (mG)	990	1200
M_A	11.4	11.9
θ	5°	35°

C in WC stars spans the range 0.2 – 0.6, with no strong sensitivity with spectral type. In this work, we assume that C/He = 0.25 by number (C= 0.4 by mass), as the ratio of C IV 5471/He II 5411 is comparable to that in WR 90 (Dessart et al. 2000, P. Crowther, priv. communication). We note that Eenens & Williams (1992) had previously measured C/He = 0.15 for WR 140. The O abundance in WC stars is also poorly constrained, though the number ratio of O/He is estimated as 0.03 ± 0.01 for WR 90 (WC7) and WR 135 (WC8) (Dessart et al. 2000). Since Hillier & Miller (1999) had earlier obtained O/He=0.1 for WR 111 (WC5), we adopt O/He = 0.05 (O = 0.1 by mass). Our values for C/He and O/He lie within the range considered by Pollock et al. (2005), while we note that in comparison Zhekov & Skinner (2000) adopt C and O abundances which are below the lower end of the ranges noted above. With these assumptions, the mass fractions of hydrogen, helium, and “metals” (X , Y , and Z respectively) for the WC7 wind are $X = 0.0$, $Y = 0.5$, $Z = 0.5$. Solar abundances are assumed for the O star (mass fractions $X = 0.705$, $Y = 0.275$, $Z = 0.020$). Both winds are assumed to have a temperature of 10,000 K, with an ionization structure of H $^+$, He $^+$, and CNO $^{2+}$.

4.2.2 Collisionless shocks - electron thermalization, non-equilibrium ionization, and shock modification

Previous models of the X-ray emission from the WCR in wide CWB systems have usually assumed that the shocks are collisional, with immediate equilibration of the

post-shock electron and ion temperatures. However, in reality they are collisionless (e.g., Draine & McKee 1993), and there is growing observational evidence that in such shocks the ratio of post-shock electron to ion temperature, T_e/T_i , is a function of the shock speed (e.g., Rakowski 2005). Temperature equilibration through Coulomb collisions and plasma instabilities then occurs some distance downstream. This process has been examined in WR 140 by Zhekov & Skinner (2000) and by Pollock et al. (2005), and can naturally account for the observed soft X-ray continuum emission. Since the ionization timescale is of the same order as the timescale for energy transfer from ions to electrons, it is not surprising that observations of WR 140 also indicate that the post-shock plasma has yet to reach ionization equilibrium (Pollock et al. 2005), and that line-profile models which assume rapid ionization equilibrium (Henley, Stevens & Pittard 2003) are unable to reproduce the observed correlation of X-ray line widths with ionization potential (Henley 2005).

Despite this progress, the physics of the heating process in the shock layer remains poorly understood, and shocks which are efficient at accelerating particles may equilibrate their electron and ion thermal populations more rapidly, in addition to reducing the equilibrium value of T_e and T_i (Ellison, Decourchelle & Ballet 2004). In this case, the X-ray spectrum is softened due to the reduction in the post-shock electron temperature behind a weaker subshock (see Fig. 1). It is unclear whether, and to what extent, shock modification may occur in WR 140, but this mechanism could potentially play some role in creating the low value of T_e observed. A simple calculation reveals that even if particle acceleration is highly efficient, the non-thermal particles in the precursor would have a negligible effect on the ionization of the pre-shock gas, consistent with the observed lack of line emission near the wind terminal speeds (Pollock et al. 2005).

A full understanding of WR 140’s spectrum will eventually require a detailed hydrodynamical model which accounts for the large post-shock equilibration timescales of the plasma ionization and electron and ion temperatures, combined with the acceleration of non-thermal particles and their effect on the shocks bounding the WCR and both the upstream and downstream flow (e.g., Pollock et al. 2005). As the development of such models is not trivial, here the synthetic X-ray spectra are calculated from models of unmodified collisional shocks. Given this simplification and the uncertainties described above, we adopt a rather pragmatic approach, and concentrate on obtaining a comparable flux at ~ 3 keV. Absorption is negligible at this energy at the chosen phase (see Fig. 18) for reasonable viewing angles, while at higher energies the relative softness of the observed emission is clear evidence for $T_e < T_i$, with the (less likely) possibility that shock modification also plays a role (see Fig. 4).

The fact that the thermal X-ray luminosity from the WCR, L_x , scales as \dot{M}^2 when the post-shock gas is largely adiabatic means that even if shock modification occurs, and were to lead to fairly substantial (e.g., factor of two) changes in L_x , mass-loss rates derived from models with unmodified shocks will be much less affected. Moreover, the inferred mass-loss rates are largely insensitive to the assumption of $T_e = T_i$. For instance, setting $T_e = 0.5T_i$ throughout the entire WCR reduces the emission at 3 keV by 23% com-

pared to a model with $T_e = T_i$. An increase of only 14% in the mass-loss rates is required for the original flux to be regained. In this way we can still obtain useful estimates of the stellar mass-loss rates from the modelling work which follows.

4.2.3 WR mass-loss rate from thermal X-ray models

Having specified the composition of the winds (Sec. 4.2.1) and unmodified, collisional shocks (Sec. 4.2.2), theoretical calculations of the X-ray emission, based on axisymmetric 2D simulations of the stellar winds and the WCR, can now be made. The X-ray emissivity is calculated using the MEKAL emission code (Mewe, Kaastra & Liedahl 1995, and references therein) for optically thin thermal plasma, and ionization equilibrium and rapid thermalization of the electrons is assumed.

The intrinsic (i.e. prior to any absorption) X-ray emission calculated from a model of the WCR with a fixed WC7 mass-loss rate, but for two different values of η , is shown in Fig. 3. As η increases, the X-ray flux increases, as explained earlier. Clearly, in order that the X-ray flux calculated from hydrodynamical models of the WCR is comparable to observations, the mass-loss rate of the WC7 star must be adjusted as η is varied.

There have been a number of X-ray observations of WR 140 in recent years, and we choose to use an ASCA observation taken on Dec. 20 1999 ($\phi = 0.837$). At this phase the X-ray luminosity is climbing rapidly (Pollock, Corcoran & Stevens 2002), while the radio emission is around its maximum intensity, and the stellar separation, ($D = 3.13 \times 10^{14}$ cm, see Dougherty et al. 2005), is sufficiently large that the shocked gas in the WCR is approximately adiabatic, allowing easy adjustment of the model mass-loss rates in order to obtain a specific X-ray flux. The mass-loss rates required to match the observed X-ray emission at $\phi = 0.837$, as a function of η , are noted in Table 2. Fig. 4 demonstrates that the X-ray emission from two of these models is comparable to the observed emission at ~ 3 keV, as required. Models of the radio emission (Sec. 4.3.2) indicate η is likely to have a value near the lower end of the range covered by Table 2. This implies the mass-loss rate of the O4-5 supergiant in WR 140 is lower ($\approx 8 \times 10^{-7} M_\odot \text{ yr}^{-1}$) than the suggested values in Repolust et al. (2004) ($8.6 - 8.8 \times 10^{-6} M_\odot \text{ yr}^{-1}$). However, an order of magnitude reduction in the mass-loss rate is consistent with the recent estimates of Fullerton, Massa & Prinja (2006).

We note that Pollock et al. (2005) determine $\dot{M}_{\text{WR}} \sim 1.5 \times 10^{-5} M_\odot \text{ yr}^{-1}$ from the degree of circumstellar absorption observed by Chandra near periastron. While this value is independent of the clumping in the winds, it is likely to be a lower limit since the overall absorption of emission from the WCR is probably somewhat less than occurs for emission near the apex of the WCR. This method will also underestimate \dot{M}_{WR} if there are regions of O star wind between the observer and the WR star at this phase due to the curvature of the WCR induced by the orbital motion of the stars. Therefore, it is argued that the range of values of \dot{M}_{WR} considered in our models is consistent with this constraint (see Table 2), and does not preclude values of η as low as 0.02.

Due to the relatively low abundance of C and O assumed by Zhekov & Skinner (2000), their derived mass-loss

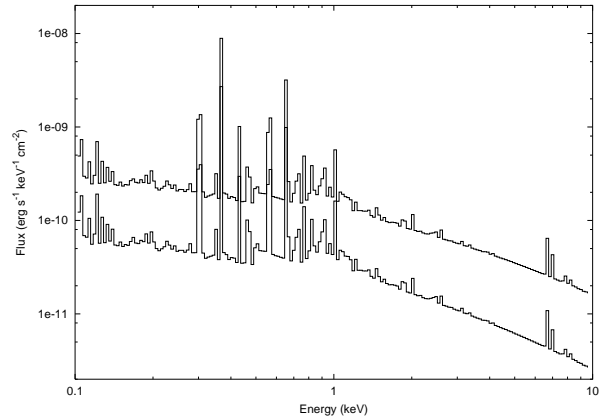


Figure 3. Comparison of the intrinsic thermal X-ray emission calculated from hydrodynamical models of the WCR in WR 140 at $\phi = 0.837$ for two different values of η , assuming unmodified collisional shocks (Sec. 4.2.2). $\eta = 0.22$ (top) and $\eta = 0.0353$ (bottom). In these calculations the mass-loss rate of the WC7 star and the terminal wind speeds were fixed ($\dot{M}_{\text{WR}} = 4.3 \times 10^{-5} M_\odot \text{ yr}^{-1}$, $v_{\infty, \text{WR}} = 2860 \text{ km s}^{-1}$, $v_{\infty, \text{O}} = 3100 \text{ km s}^{-1}$), while the mass-loss rate of the O star was varied according to the desired value of η . The continuum flux is also sensitive to the adopted abundance of the WR wind (see Sec. 4.2.1).

Table 2. The mass-loss rates (in units of $10^{-6} M_\odot \text{ yr}^{-1}$) required to match the observed X-ray flux at 3 keV and $\phi = 0.837$ as a function of η . Column 4 indicates lower limits for the volume filling factor, f , of clumps in the winds, as determined from a comparison between the X-ray and radio derived mass-loss rates (Sec. 4.2.4). For simplicity, we assume that the two winds have the same values of f . Recent analyses of O star winds indicate that $f \sim 0.02 - 0.1$ (see Fullerton, Massa & Prinja 2006, and references therein). Columns 5-7 note approximate values of θ for which the sight lines are parallel to the asymptotic opening angles of the WR shock, contact discontinuity, and O shock.

η	\dot{M}_{WR}	\dot{M}_{O}	f	θ_{WR}	θ_{CD}	θ_{O}
0.02	43.3	0.80	0.199	41°	59°	90°
0.0353	33.3	1.09	0.118	35°	54°	79°
0.055	27.2	1.38	0.079	30°	49°	71°
0.0825	23.2	1.76	0.057	25°	42°	65°
0.11	20.2	2.05	0.043	19°	38°	56°
0.16	17.2	2.54	0.031	11°	32°	52°
0.22	14.9	3.02	0.024	4°	27°	48°

rates for $\eta = 0.0353$ are higher than ours (cf. their model A and AA), even though the system distance has since been revised upwards. We also note that the wind parameters noted in Dougherty et al. (2005) overpredict the observed X-ray emission by a factor of about 8.

Given the existing uncertainties with respect to the degree of shock modification, and the amount of post-shock electron heating and the timescale for electron and ion temperatures to reach equilibrium, Fig. 4 demonstrates that it is difficult to uniquely determine the WR star mass-loss rate and η from the X-ray spectrum alone. While a simpler, and perhaps a more reliable, method of determining η in CWB systems with highly eccentric orbits involves utilizing the du-

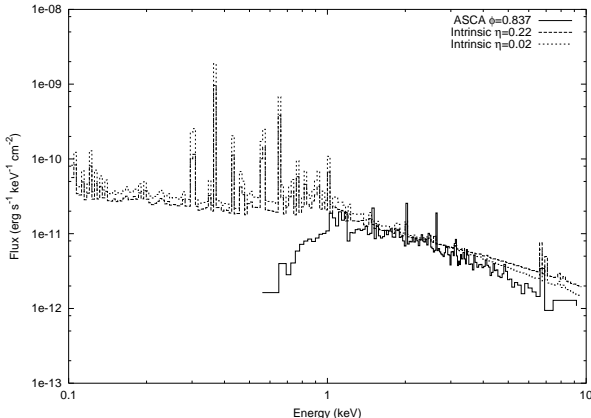


Figure 4. The intrinsic thermal X-ray emission from hydrodynamical models of the WCR at orbital phase $\phi = 0.837$ with $\eta = 0.22$ (dashed) and $\eta = 0.02$ (dotted). There is a slight decrease in the hardness of the model spectra with η , as expected. Also shown is the observed X-ray emission (solid). The X-ray emission from the models (at 3 keV) is comparable to the observed emission, though the latter is softer. As discussed in Sec. 4.2.2, this is primarily because $T_e < T_i$.

ration of any X-ray “eclipse” (see, e.g., Pittard & Corcoran 2002), the very short eclipse seen in the lightcurve of WR 140 (Pollock et al. 2005) means that a detailed analysis using 3D hydrodynamical simulations is probably needed. Therefore, we turn to the high quality radio spectra now available to further constrain η (Sec. 4.3.2).

4.2.4 Wind clumping

There is now considerable observational evidence that the winds of massive stars are clumpy (e.g., Crowther et al. 2002; Hillier et al. 2003; Massa et al. 2003; Repolust et al. 2004; Fullerton, Massa & Prinja 2006; Owocki & Cohen 2006). Additional support is provided by models of radiatively-driven winds. Clumping affects the thermal radio emission from the unshocked winds, though simple arguments suggest that in wide binaries, where the WCR is largely adiabatic, clumps are rapidly destroyed upon encountering the WCR (Pittard et al. 2006). Therefore, in the following models we assume that the unshocked winds are clumpy (with the same degree of clumping for both winds), and the WCR smooth.

The degree of clumping may be conveniently parameterized by a volume filling factor, f , where it is assumed that the clumps occupy a fraction f of the wind volume, with the interclump medium being of negligible density. Radio-derived mass-loss rates of clumpy winds are related to those of smooth winds by $\dot{M} = \dot{M}_{\text{smooth}}/f^{1/2}$, since the thermal flux S_{ff} increases accordingly (see, e.g., Eq. 16 in Pittard et al. 2006). This relationship is more complicated in binaries, as the degree of clumping may be different for each wind, and the thermal emission from the WCR may make a non-negligible contribution to the total thermal emission (see Fig. 11 in Pittard et al. 2006). Nevertheless, we proceed by assuming the WR wind dominates the thermal radio emission in WR 140, so that a value for f can be deduced from a comparison of the X-ray and radio derived mass-loss

rates. The unclumped estimate of $5.3 \times 10^{-5} M_{\odot} \text{ yr}^{-1}$ from Williams et al. (1990) translates into $9.7 \times 10^{-5} M_{\odot} \text{ yr}^{-1}$ for a system distance of 1.85 kpc, and leads to the lower limits for f noted in Table 2. An additional uncertainty is that the mass-loss rate of Williams et al. (1990) assumes the radio flux at $\phi = 0.0$ is entirely thermal, which is far from clear. While such assumptions should be avoided if at all possible, our approach is conservative in the sense that the theoretical thermal flux from the unshocked winds cannot exceed the measured flux at periastron. Since the total observed flux at $\phi = 0.837$ is $\sim 20 \times$ greater at 5 GHz and $\sim 5 \times$ greater at 22 GHz than our estimate of the thermal flux, the models in Sec. 4.3.2 should not be overly sensitive to our choice of f , although p will be overestimated slightly if the thermal flux is in fact lower than assumed. Wind clumping also affects the radius of the $\tau = 1$ surface (see Eq. 17 in Pittard et al. 2006). In the clumpy WR wind in our models, $R_{\tau=1}$ has values of 8.8, 4.0, and 1.8×10^{14} cm at 1.6, 5, and 15 GHz. This is independent of the variation in \dot{M}_{WR} with η due to the corresponding variation in f .

4.3 Models of the radio data

We concentrate on obtaining reasonable spectral fits to the radio data at the same orbital phase ($\phi = 0.837$) we determined potential values for stellar mass-loss rates and corresponding values of η from the observed X-ray emission (see Sec. 4.2.3). The brightness temperature of the radio emission is $\approx 3 \times 10^7$ K at this phase, so the observed emission is dominated by non-thermal processes (Dougherty et al. 2005). Therefore, a good estimate of the population of relativistic electrons can be obtained, allowing predictions of the non-thermal X-ray and γ -ray emission. We will apply our modelling to a variety of orbital phases in a forthcoming paper.

There are several free parameters used to fit the observed radio emission, including η , the index of the non-thermal electron energy distribution, p , and $\zeta_{\text{rel},e}$ and ζ_B , which normalize the model spectra and the magnetic field strength (and hence the impact of the Razin effect). The effect of reducing the luminosity of the stars is also investigated. The line of sight angle into the system at $\phi = 0.837$ is specified by the orbit derivation of Dougherty et al. (2005) as $\theta = 52^\circ$, though the uncertainty in this value is large ($\sim 10^\circ$) and we allow θ to vary substantially ($\pm 10 - 20^\circ$) in our models.

4.3.1 Parameter study

Before attempting a fit to the $\phi = 0.837$ data, it is instructive to examine how the model spectra vary with θ , η , p , ζ_B , and L_{bol} . Fig. 5 shows how the model *synchrotron* spectra change as θ (and hence the free-free absorption along the line of sight) is varied, for models with $\eta = 0.11$, $p = 2.0$, $\zeta_{\text{rel},e} = 0.215$, and $\zeta_B = 2.6 \times 10^{-4}$. The Razin effect produces a turnover at about 2.3 GHz, while the high frequency emission from each model tends to the same slope as the free-free attenuation becomes negligible. The sensitivity of the spectrum at low frequencies to changes in θ is expected since the size of the radio photosphere is larger than the stellar separation. At high frequencies the radio

photosphere is smaller and has a commensurately weaker influence on the absorption of emission from the WCR. The synchrotron emission is least affected by free-free absorption when $\theta \approx 20^\circ$ (i.e. when the lines of sight are roughly parallel to the asymptotic angle of the WR shock), and the turnover frequency is the same as that of the intrinsic synchrotron emission. A dramatic increase in the level of free-free absorption occurs as θ decreases and the WR wind moves in front of the WCR, with maximum absorption at $\theta = -90^\circ$ (i.e. WR star in front). For $\theta \lesssim 20^\circ$, free-free absorption causes the low frequency turnover. As the line of sight swings through the WCR from the WR shock to the O shock i.e. $\theta = 20^\circ \rightarrow 56^\circ$, the level of absorption again increases, although in a somewhat complicated fashion as the source is extended and there are multiple lines of sight. While free-free absorption determines the slope of the spectrum between 3 and 20 – 30 GHz, it is only between 50° and 60° , when the sight lines move out of the WCR and into the O wind, that the turnover due to free-free absorption dominates over the Razin effect, and the turnover becomes very broad. The turnover frequency increases as the O wind moves in front of the WCR i.e. as $\theta \rightarrow 90^\circ$. The smaller stellar separation in the models presented here results in free-free absorption having an influence to much higher frequencies than in the models shown in Fig. 10 of Dougherty et al. (2003).

It is interesting to note that when the sight lines are through the WCR, a turndown or “kink” is visible in the spectrum at a few 10’s of GHz (this is most clearly seen when $\theta = 50^\circ$). Typically, such turndowns are attributed to a change in the non-thermal energy spectrum. However, it is certainly not the cause here, because the intrinsic synchrotron spectrum does not display such a kink (although spectral breaks from IC cooling occur in our models, the break frequency is spatially dependent, and is smoothed out once the flux is integrated over the entire WCR - see Fig. 3 in Pittard et al. 2006). It is clear that lines of sight through the WCR are optically thin at frequencies above 20-30 GHz, and almost all, if not all, the synchrotron emission from the WCR is seen.

The variation of the spectra as a function of η is shown in Fig. 6, where the total emission (synchrotron plus free-free) is displayed. In this and the following figures, emission between 0.5 and 50 GHz is examined, since this is approximately the frequency range of the observations. The spectral variations in Fig. 6 bear some resemblance to the changes with θ , since as η varies, the relative angle of the sight lines to the WCR changes if θ is fixed. For $\eta = 0.055 - 0.16$, the line of sight is through the lower opacity WCR. When $\eta = 0.22$, it is through the unshocked O wind, and the synchrotron emission from the WCR suffers more free-free absorption than seen in the other models, which results in the low frequency turnover occurring at a higher frequency (c.f. Fig. 5). For the remaining models, the reduced level of free-free absorption means that the turnover is the result of the Razin effect, and therefore occurs at approximately the same frequency in each case (since ζ_B is fixed). It is clear from Fig. 6 that the spectral slope between 10-40 GHz steepens as η decreases (the slight upward curvature in the $\eta = 0.055$ model near 40 GHz is caused by rising free-free emission), which is due to the change in the relative angle of the sight lines with respect to the WCR, as seen in Fig. 5, and the resulting change in the free-free opacity. While Fig. 6 does not show

frequencies as high as Fig. 5, the synchrotron emission tends to a similar slope in all models (since p is the same in each model) with a slight steepening as η decreases due to the WCR moving closer towards the O star, and the amount of IC cooling increasing.

Fig. 7 shows the effect of varying the slope of the non-thermal electron energy distribution. As p decreases, the slope of the intrinsic synchrotron emission increases, resulting in flatter attenuated spectra. Fig. 8 illustrates the effect of changing ζ_B . As ζ_B is reduced, the spectral index above 4 GHz increases. By decreasing ζ_B (and thus B), the synchrotron emission at a given frequency arises from non-thermal electrons with higher Lorentz factors ($\nu \propto \gamma^2 B$), and thus sample a steeper slope for the non-thermal electron energy distribution due to the increased impact of IC cooling at high γ (see Fig. 3 in Pittard et al. 2006). At very low values of ζ_B , the Razin effect becomes the dominant mechanism responsible for the low frequency turnover in Fig. 8.

The effect of adjusting the stellar luminosities is shown in Fig. 9. For simplicity, the luminosity of both stars is adjusted by the same amount, although the amount of IC cooling is primarily determined by the luminosity of the O supergiant. In our model, a power-law distribution of non-thermal electrons is injected along the entire shock front with the same initial spectral index and normalization (relative to the local post-shock thermal energy density - see Sec. 2.2.1). Near the apex of the WCR, there is strong IC cooling but the cooling weakens away from the apex as the stellar radiation field density diminishes, and the non-thermal particles can maintain higher energies. As the L_{bol} values are reduced, the influence of IC cooling decreases, the non-thermal electrons are able to keep higher energies throughout the WCR, and the population of the highest energy electrons can exist throughout a larger part of the WCR. The result is that the spectrum of synchrotron emission, summed over the entire WCR, becomes less steep. Clearly a specific spectral slope can be obtained with a larger value of p if the model values of L_{bol} are reduced. For a given energy density of non-thermal electrons immediately post-shock, a reduction in IC cooling also produces an increase in the overall flux. It is conceivable that the assumptions in Sec. 4.2 may overestimate the stellar luminosities, but with one exception the models in the rest of this work are based on the luminosities noted in Table 1.

We have also investigated what happens to the observed synchrotron emission if the emission region is limited to $r < \pi r_O/2$, as suggested by Eichler & Usov (1993). We find that the spectral index is essentially unchanged, and thus our fits for p are robust in this context, though the flux is diminished to 40 – 75% of its previous value due to the reduced size of the emitting region.

4.3.2 Spectral fits at $\phi = 0.837$

Our initial aim was to determine parameter values directly from model fits to the radio data. Unfortunately, reasonable fits to the data are possible with a range of parameters. For example, by varying p and θ similar fits are attained over a wide range of η . Furthermore, the data can be fit with either free-free absorption or the Razin effect responsible for the low frequency turnover. However, despite this degeneracy of models, it is possible to discriminate between models by

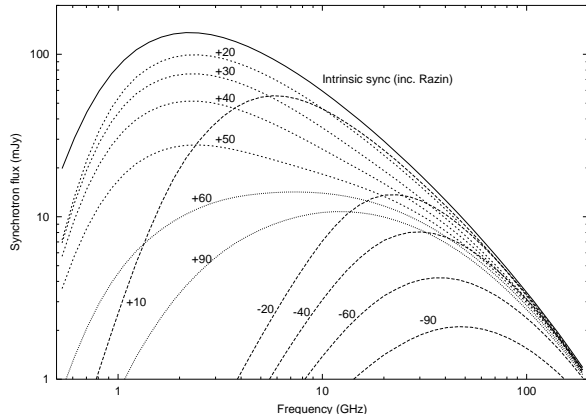


Figure 5. The influence of θ on the observed *synchrotron* emission. All models have $\eta = 0.11$, $p = 2.0$, $\zeta_{\text{rel,e}} = 0.215$, and $\zeta_B = 2.6 \times 10^{-4}$. The lines of sight are through the WR wind when $-90^\circ < \theta \lesssim 19^\circ$, through the WCR when $19^\circ \lesssim \theta \lesssim 56^\circ$, and through the O wind when $56^\circ \lesssim \theta < 90^\circ$, as indicated by the long-dashed, short-dashed, and dotted lines respectively (see Table 2). The intrinsic synchrotron emission is indicated by the solid line.

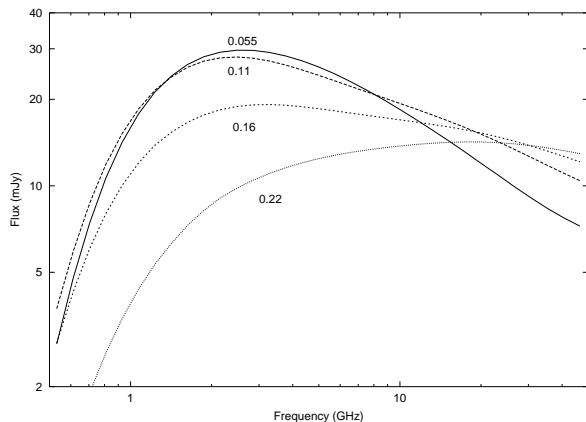


Figure 6. The influence of η on the model radio spectra. IC cooling and the Razin effect are included in these calculations. Ionic cooling and synchrotron self-absorption are negligible. All models have $\theta = 50^\circ$, $p = 2.0$, $\zeta_{\text{rel,e}} = 0.215$, and $\zeta_B = 2.6 \times 10^{-4}$, though the mass-loss rates and f were varied according to Table 2. The line of sight is through the WCR in all models except for $\eta = 0.22$, when it is through the unshocked O star wind. The synchrotron emission from the WCR dominates the free-free emission from the winds and WCR for the chosen parameters.

using other properties, such as the values of θ and $\zeta_{\text{rel,i}}$ required by each model, which we discuss later in this section. Parameters for a variety of model fits are listed in Table 3.

Two model fits which span the range of η considered are shown in Fig. 10. For both of the models in Fig. 10, $\zeta_B = 0.05$ was assumed. Sightlines which have θ marginally less than θ_{WR} are necessary for free-free absorption to cause the low frequency turnover. With these restrictions, $p = 1.4$ is needed to match the slope of the data points between 5 and 22 GHz. Fits with free-free absorption dominant over Razin cannot be obtained when the sightlines are through the WCR because the free-free absorption is too low, while

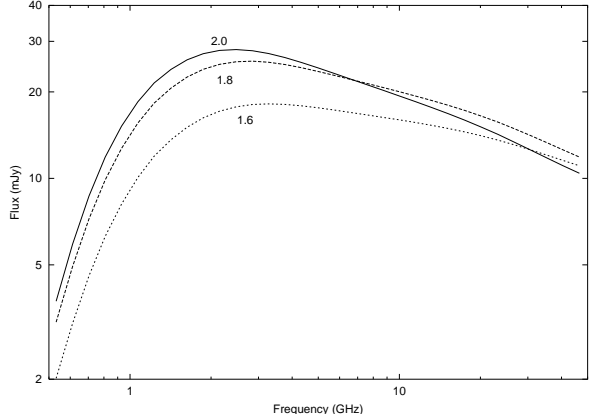


Figure 7. The influence of p on the model radio spectra. All models have $\eta = 0.11$, $\theta = 50^\circ$, $\zeta_{\text{rel,e}} = 0.215$, and $\zeta_B = 2.6 \times 10^{-4}$, and the line of sight is through the WCR.

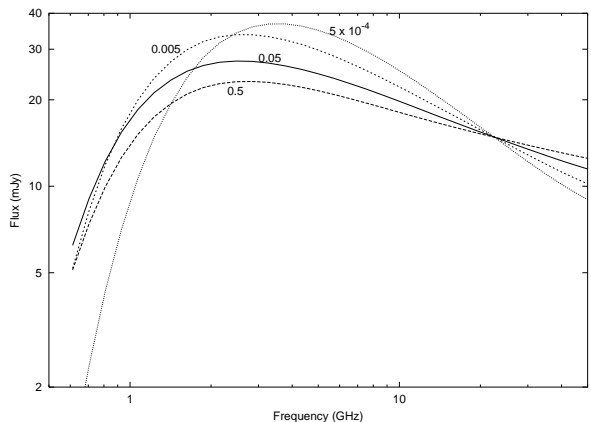


Figure 8. The influence of ζ_B on the model radio spectra. All models have $\eta = 0.0353$, $p = 1.4$, and $\theta = 27^\circ$, and the line of sight is through the unshocked WR wind. $\zeta_{\text{rel,e}}$ was adjusted in each model to obtain a specific flux at 22 GHz.

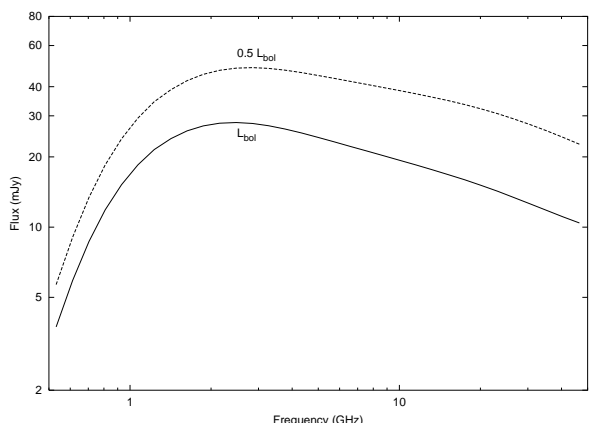


Figure 9. The influence of the stellar luminosities on the model radio spectra. Both models had $\eta = 0.11$, $p = 2.0$, $\zeta_{\text{rel,e}} = 0.215$, $\zeta_B = 2.6 \times 10^{-4}$, and $\theta = 50^\circ$, and the line of sight is through the WCR.

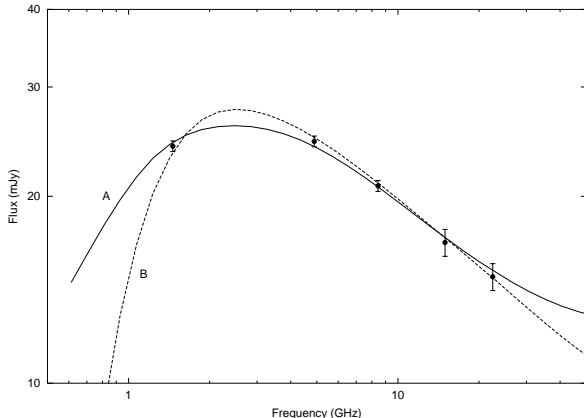


Figure 10. Model fits to radio data of WR 140 at $\phi = 0.837$. In these models, which span the range of η considered, the low frequency turnover is due to free-free absorption. The data are represented by solid circles, with fluxes taken from Table 2 of Dougherty et al. (2005); in this and subsequent figures we assume that the uncertainty in the absolute flux scale is 5% for $\nu \geq 15$ GHz and 2% for $\nu < 15$ GHz (Perley & Taylor 2003). The model parameters are noted in Table 3, and the line of sight is through the unshocked WR wind. Model A has $\eta = 0.22$, while model B has $\eta = 0.02$. The low frequency turnover is shallower in model A, and the high frequency total emission has a stronger concave curvature, relative to model B. The variation of the high frequency emission is due to differences in the slope of the synchrotron and free-free emission in both models. The thermal flux from the unshocked winds and the WCR is ≈ 4 mJy at 50 GHz in both models.

sightlines through the unshocked O wind require $p \gtrsim 2.5$ for the non-thermal electron distribution to offset the synchrotron spectrum between 5-22 GHz becoming flatter as $\theta \rightarrow 90^\circ$ and the free-free opacity increases (cf. Fig. 5). While such values of p are appropriate for modified shocks, the required values of θ are much too high compared to the value of 52° determined by the orbital solution of Dougherty et al. (2005). In fact, we find that all model fits with $p > 2$ are unsatisfactory, with either $\zeta_{\text{rel},e}$ or θ being uncomfortably high.

Since the opening angle of the WCR varies with η , the value of θ required to match the low frequency synchrotron turnover varies in a similar fashion. For the models in Fig. 10, θ is 5° for model A and 35° for model B (acceptable fits with η between 0.02 and 0.22 can also be obtained). The value of θ from model A is inconsistent with the 52° determined by Dougherty et al. (2005) at this phase, and while in model B it is still different by some considerable margin, it is not entirely implausible given the large uncertainty that exists for θ . It is anticipated that models with $\eta < 0.02$ should result in fits with θ closer to the value determined by Dougherty et al. (2005), but η is not expected to be lower than ~ 0.01 because the mass-loss rate of the WR star then becomes too large.

The slope of the high frequency synchrotron emission is sensitive to both p (Fig. 7) and ζ_B (Fig. 8). Since there is almost complete degeneracy between these parameters, a variety of fits with different families of p and ζ_B can be obtained (Fig. 11). For a given η , the value of θ required to match the low frequency turnover is largely unchanged

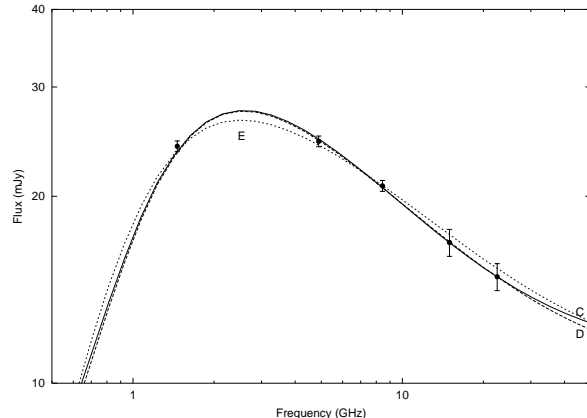


Figure 11. Model fits to the radio data at $\phi = 0.837$, again where the low frequency turnover is due to free-free absorption (models C, D, and E). Due to the sensitivity of the slope of the high frequency synchrotron emission to both p and ζ_B , it is possible to obtain, for a given η , fits of similar quality with different values of p and B . All models had $\eta = 0.11$ (see Table 3).

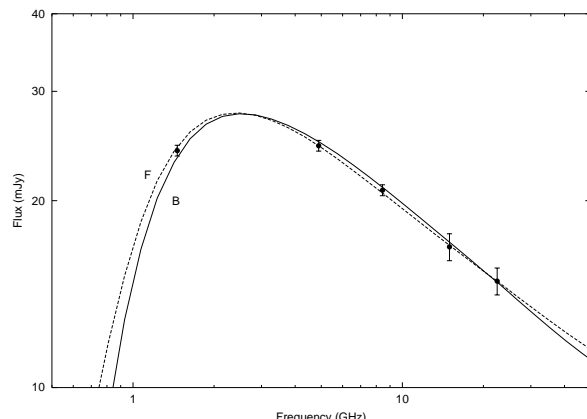


Figure 12. Models of the radio data at $\phi = 0.837$ which demonstrate that it is possible to obtain fits of similar quality with a higher value of p when the stellar luminosities are reduced. Both models (B and F) had $\eta = 0.02$ and $\zeta_B = 0.05$ (see Table 3).

in these fits. If the stellar luminosity is reduced, fits with a higher value of p can be obtained, as shown in Fig. 12. However, we are unable to fit the data with $\eta = 0.02$ and $p = 2$, despite making the other parameters as favorable as possible for this task (e.g., $\zeta_B = 0.05$ and luminosities reduced by a factor of two).

As already noted, we are also able to obtain reasonable fits to the data when the Razin effect is responsible for the low frequency turnover. Again, fits of similar quality can be obtained across a wide range of η and p , as demonstrated in Fig. 13. In these models an attempt was made to match θ as closely as possible to the value determined from the orbital solution of Dougherty et al. (2005).

Before the relative merits of the models with either the Razin effect or free-free absorption being responsible for the low frequency turnover are considered, it is worth looking at the make-up of each of these models. The intrinsic synchrotron (i.e. before circumstellar absorption) and the free-

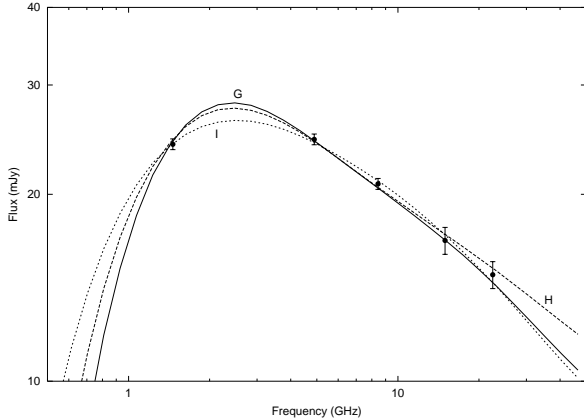


Figure 13. Model fits to the radio data at $\phi = 0.837$ where the low frequency turnover is due to the Razin effect (models G, H, and I). The model parameters are again noted in Table 3.

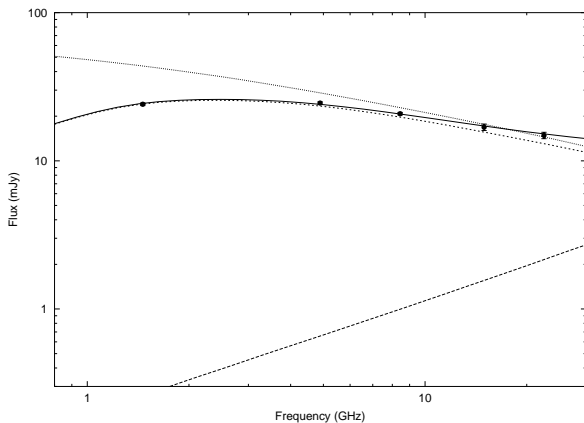


Figure 14. The amount of free-free absorption affecting the intrinsic synchrotron emission in model A, where the low frequency turnover is due to free-free absorption. Various emission components are shown - free-free flux (long-dashed), synchrotron flux (short-dashed), intrinsic synchrotron flux (dotted), and total flux (solid). The spectral index of the intrinsic synchrotron emission is -0.34 between 1.5 and 5 GHz, and steepens to -0.47 between 15 and 22.5 GHz. This illustrates the effect of IC cooling, since, for $p = 1.4$, $\alpha = -0.2$ is expected.

free emission components to the total flux for model A where the low frequency turnover is due to free-free absorption are shown in Fig. 14. The free-free flux is negligible in comparison to the synchrotron flux, which only suffers significant absorption at low frequencies. In this case, the observed synchrotron luminosity between 1 - 40 GHz is roughly 90% of the intrinsic synchrotron luminosity. Somewhat paradoxically, the intrinsic synchrotron emission from models where the low frequency turnover is caused by the Razin effect can experience more severe free-free absorption, as seen from a comparison of Figs. 14 and 15. This is because the free-free absorption is smallest when the sight lines are closely parallel to the WR shock (as is the case for model A), and is significantly greater when the sight lines are deeper within the WCR (e.g., compare the 10 GHz flux in Fig. 5 when $\theta = 10$ or 20° with the flux when $\theta = 40^\circ$ - see also the dot-

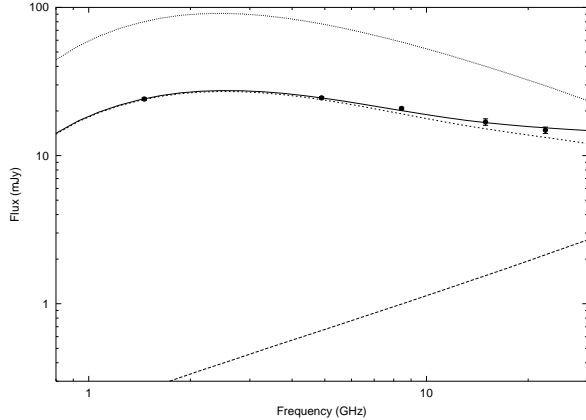


Figure 15. As Fig. 14 but for model J, where the Razin effect is responsible for the low frequency turnover.

Table 3. Parameters for model fits to the $\phi = 0.837$ radio data. In models A-F the low frequency turnover is due to free-free absorption, while in models G-J it is due to the Razin effect. The values of θ for which the sight lines are parallel to the asymptotic opening angle of the WR shock, contact discontinuity, and O shock are noted in Table 2.

Model	η	p	$\zeta_{\text{rel,e}}$	ζ_B	θ
A	0.22	1.4	1.38×10^{-3}	0.05	5°
B	0.02	1.4	5.36×10^{-3}	0.05	35°
C	0.11	1.53	2.26×10^{-4}	0.5	13°
D	0.11	1.4	2.03×10^{-3}	0.05	13°
E	0.11	1.1	2.79×10^{-2}	5.0×10^{-3}	14°
F	0.02	1.6	1.81×10^{-3}	0.05	40°
G	0.11	2.0	0.22	2.6×10^{-4}	50°
H	0.11	1.6	0.15	4.0×10^{-4}	44°
I	0.0353	1.4	0.14	1.0×10^{-3}	58°
J	0.22	1.5	0.14	4.0×10^{-4}	36°

ted curve in Fig. 12b in Pittard et al. 2006). The observed synchrotron luminosity in Fig. 15 is only 40 per cent of the intrinsic synchrotron luminosity, and in such cases the IC luminosity predicted using Eq. 3 will be substantially underestimated if the absorption is not accounted for.

4.3.3 Synthetic radio images

The spatial distributions of radio emission from models A and B are shown in the left and right panels of Fig. 16. In all panels the intensity of emission from the WCR exceeds that from the stars, though the relative amount of free-free emission increases strongly with frequency. Model A is viewed at low inclination, while model B is viewed at a somewhat higher inclination (Table 3). The absorption of emission from the far side of the WCR by the O wind is negligible in model A, but significant in model B, as evident by the dearth of emission near the O star. As expected, this hole is much larger at 1.7 GHz than at 8.4 GHz. The O star is not located at the centroid of the hole, since the O wind is restricted on one side by the WCR. Those parts of the WCR with optically thin lines of sight through the outer envelope of the “modified” O wind are predominantly observed. In

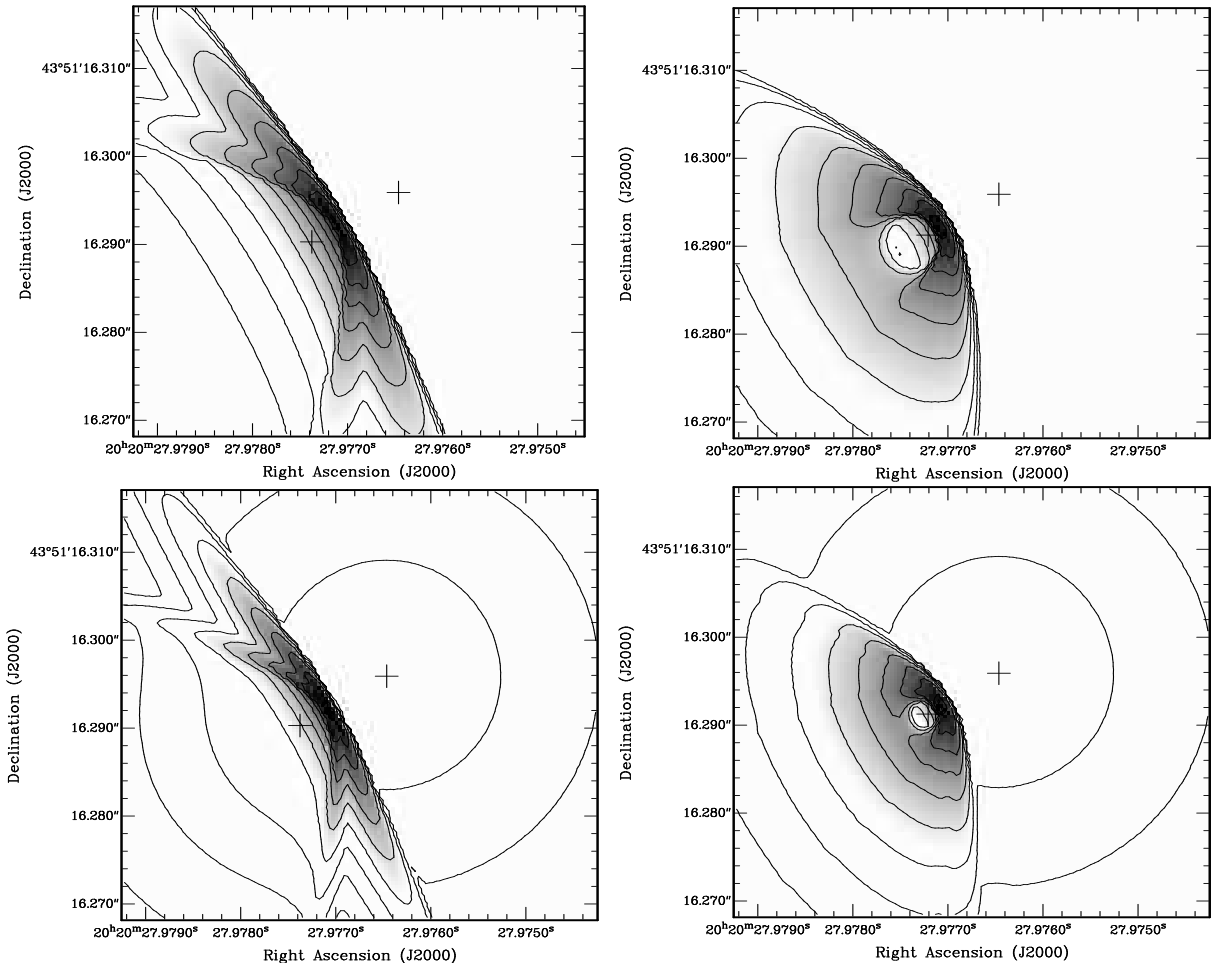


Figure 16. Intensity distributions at 1.7 GHz (top) and 8.4 GHz (bottom) from model A (left) and model B (right) of WR 140. The contour levels are spaced apart by 0.5 dex, are chosen to highlight the large-scale structure, and are identical in both model's at a specific frequency, though change with frequency. The positions of the stars are indicated by crosses (WR star to the upper-right of the O star). The effect of different wind momentum ratios and line of sight angles are clearly visible.

addition, the intensity of the far side of the WCR is highest nearer the apex. The reduced opening angle of the WCR in model B relative to model A is clearly visible. IC cooling creates a “V”-shaped intensity distribution in model A, but this is not so clearly seen in model B, largely due to the difference in viewing angle.

Though not shown here, another important finding is that the relative position of the stars and the observed peak of the emission from the WCR is not necessarily related to η , due to the occultation of the WCR by the O star stellar wind. In fact, as θ increases and D decreases the absorption can become so large that the position of the WCR apex appears closer to the WR star than to the O star, despite the WR star having the stronger wind. Finally, we note that no offset between the center of emission at 1.7 GHz and 8.4 GHz is seen, contrary to the report by Dougherty et al. (2005).

To more closely compare the model intensity distributions at 8.4 GHz to the VLBA images shown in Dougherty et al. (2005), we have used the AIPS subroutine UVCN to generate visibilities appropriate for a VLBA “observation” of our models. System noise estimates were

accounted for by including the performance characteristics of the VLBA telescopes, e.g., antenna efficiencies, system temperatures etc. The resulting visibilities are then imaged and deconvolved using standard techniques. The resulting simulated observations are shown in Fig. 17. With perfect data i.e. no noise, it is possible to distinguish the two different models (Fig. 17a). However, once appropriate noise has been incorporated, the situation is quite different as can be seen in Fig. 17b and c. Adopting the same imaging parameters (imaging weights etc.) as used in Dougherty et al. (2005), the differences between the models are not apparent. However, applying a more extreme taper to strongly emphasise the lower spatial frequency content of the visibility data (Fig. 17c) the different models can just be discerned by an apparent difference in the opening angle. These synthetic images show that any curvature in the WCR, from either free-free absorption or from the wind-momentum ratio, is at best difficult, and may be impossible, to detect with VLBI observations. It is clearly dependent on the spatial frequency content and the attainable signal-to-noise ratio of the data. The high-brightness emission that is detected by VLBI arrays arises predominantly in the vicinity of the shock apex,

where the opening angle of the shocks have yet to reach their asymptotic values. Even when the lower surface brightness emission from electrons further down the post-shock flow can be detected, e.g., by arrays with shorter baselines to recover lower spatial frequency visibilities, the beam of the array smooths out the features of the WCR. This leads us to call into question the reliability of values of η derived from these types of observation.

4.3.4 Discussion of the radio models

In attempting to identify the most suitable models, it is noted that the fits in Fig. 13 require a low B-field within the WCR ($\zeta_B \sim 3 \times 10^{-4} - 10^{-3}$), which is far from equipartition with the energy density of non-thermal particles (electrons plus ions). Assuming a simple dipole field, this implies that the B-field at the surface of each star is very low, with little or no amplification in the WCR. As the synchrotron flux is proportional to $\zeta_{\text{rel,e}} \zeta_B^{3/4}$, large values of $\zeta_{\text{rel,e}}$ are required to normalize the model spectra to the data. The models (G-J) shown in Figs. 13 and 15 imply that 10-20 % of the available wind kinetic power processed through the shocks bounding the WCR (which is a small fraction of the total kinetic power of the winds in the system) is transferred to the non-thermal *electrons*. This is unacceptably high. Hence, models where the low frequency turnover is due to free-free absorption are preferred. The high energy non-thermal emission from models G-J is also less consistent with current EGRET and INTEGRAL observations, and in model G the non-thermal X-ray flux exceeds the observed thermal flux. This is discussed further in Sec. 4.4.

Amongst models A-F, model E is notable for an extremely low value of p . The resulting high energy non-thermal spectrum is too flat if WR 140 is indeed associated with the EGRET source 3EG J2022+4317 (see Sec. 4.4.2). The magnetic energy density in model C is towards the high end of expectations, with $B = 3.3$ G at the apex of the WCR. A magnetic field this high is likely to prevent particle acceleration as the shock velocity does not exceed the phase velocity of whistler waves propagating normal to the shock (see Eichler & Usov 1993, for the necessary conditions). At this stage we also prefer to use the stellar luminosities determined in Dougherty et al. (2005), rather than reduced values such as used in model F, though further investigation of this matter is needed. On this basis, models A, B and D are preferred. Of these three models, the viewing angle of model B is closer to the value determined by Dougherty et al. (2005), and hence is the preferred model overall.

We now compare our estimate of η from model B to previous estimates. First, $\eta = 0.02$ is consistent with the value derived from Marchenko et al. (2003), from an analysis of the CIII and HeI line profiles around periastron. Dougherty et al. (2005) estimate a value an order of magnitude higher (0.22), but this is an indirect estimate based on an assumed mass-loss rate for the O supergiant. They also argue that $\eta = 0.22$ is consistent with the opening angle of the WCR as estimated from the VLBA images. However, as argued in the previous section, we should not expect the opening angle of the WCR to be constrained by the VLBA observations at this orbital phase. Varricatt, Williams & Ashok (2004), from HeI absorption in

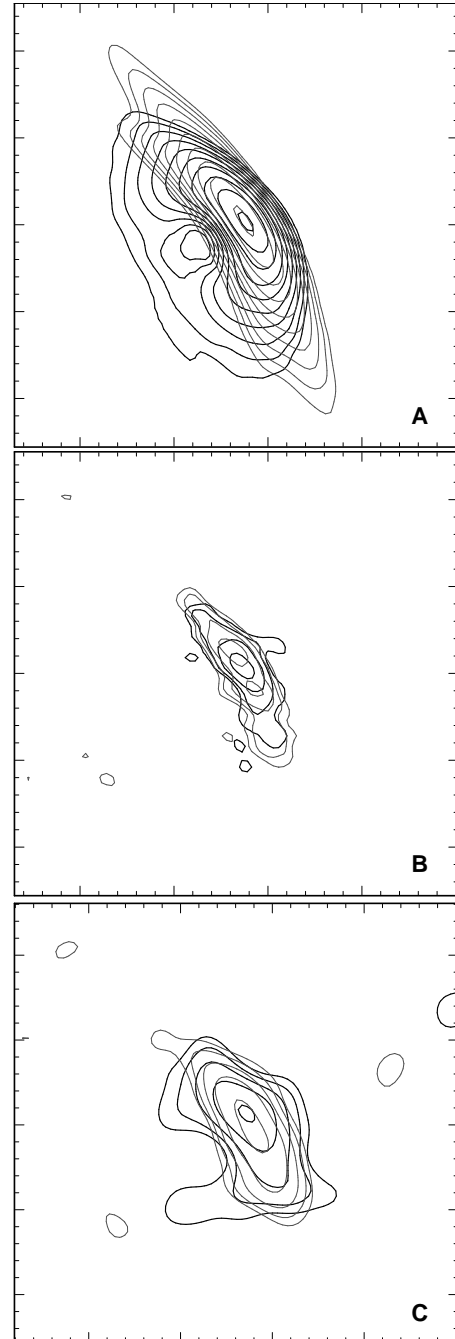


Figure 17. 8.4 GHz synthetic VLBA observations of the model intensity distributions in Fig. 16. The data have been scaled to match the peak flux in the observations in Dougherty et al. (2005) at phase 0.841 - close to $1.2 \text{ mJy beam}^{-1}$. The top panel (a) shows the resulting image for model A (thin) and model B (thick) when there is no noise i.e. “perfect” data. The middle panel (b) used the same imaging and deconvolution parameters as in Dougherty et al. (2005), and shows no discernable difference in the images of the two models. In the lower panel (c), the lowest spatial frequency content of the data is more strongly emphasized by severely tapering the data, and the two models may just be distinguished. Contours in (a) start at $30 \mu\text{Jy beam}^{-1}$ and increase by powers of 1.5. For (b) and (c), the first contour is at $33 \mu\text{Jy beam}^{-1}$. Each minor tick on the axes represents 1 mas. The scale and distribution of the emission in panel (b) is consistent with the observations at both phase 0.830 and 0.841 presented in Dougherty et al. (2005).

the WR wind, determine a lower limit to the half-opening angle of 42° , which is consistent with the value for the WR shock in model B.

4.4 The high energy emission

4.4.1 Models of the high energy emission

The parameters obtained from the models of the radio data in Sec. 4.3 allow prediction of the IC and relativistic bremsstrahlung flux, and by specifying the ratio of the energy density of electrons to ions it is possible to predict the flux from the decay of neutral pions. Such calculations can be used to further constrain the spectral index of the non-thermal particles and thus the nature of their acceleration, as demonstrated in this section.

The predicted non-thermal emission from model B is shown in Fig. 18, and a summary of the emission components noted in Table 4. The INTEGRAL flux is insensitive to reasonable assumptions about the value of γ_{\max} , though the EGRET and GLAST fluxes are more so. However, the VERITAS flux is highly sensitive to both γ_{\max} and $\zeta_{\text{rel},i}/\zeta_{\text{rel},e}$, and the predictions presented here are meant only as a guide. At GeV energies and above we may underestimate slightly the flux through our neglect of the emission from secondary particles.

The total luminosity from non-thermal processes is $\sim 0.5\%$ of the kinetic power in the wind-wind collision ($\sim 10^{36} \text{ erg s}^{-1}$), the latter being $\sim 1\%$ of the total kinetic power in the winds. The IC emission dominates for photon energies less than 50 GeV, while the emission from pion decay reaches energies up to 15 TeV (the maximum photon energy from each process is limited by the assumed value of $\gamma_{\max} = 10^5$ for the electrons and ions). The relativistic bremsstrahlung emission is a minor contributor to the total non-thermal flux, and does not dominate at any energy. The absorption of high energy photons by two-photon pair production is significant at GeV and TeV energies, in good agreement with the calculation in Fig. 2 where a single line of sight from the stagnation point of the WCR to an observer was considered.

The IC flux is directly proportional to the energy density of non-thermal electrons, $U_{\text{rel},e}$, and thus to $\zeta_{\text{rel},e}$, which in the calculation for Fig. 18 was set to 5.36×10^{-3} as determined from the fits of the radio data (Fig. 10). The gradual steepening of the IC spectrum between 2-100 keV (corresponding to $14 \lesssim \gamma \lesssim 100$) indicates the effect of IC cooling on the non-thermal electron energy spectrum. The lack of a clearly defined spectral break reflects the situation for the synchrotron spectrum at radio frequencies (see Figs. 4 and 6 in Pittard et al. 2006). Above 1 MeV, the spectral index is equal to $-p/2 = -0.7$ (corresponding to a photon spectral index, $\Gamma = -\alpha + 1 = (p+2)/2 = 1.7$).

The relativistic bremsstrahlung spectrum is fairly flat below 1 MeV, and falls off sharply at higher energies. Like the IC emission, its flux is directly proportional to the specified value of $\zeta_{\text{rel},e}$. In contrast, the emission from neutral pion decay peaks at $0.5m_{\pi}c^2 = 67.5$ MeV, and, for pions produced from collisions involving non-thermal protons, has a maximum energy of $E_{p,\max}/6$, where the maximum energy of non-thermal protons, $E_{p,\max} = \gamma_{\max}m_p c^2$. The flux from pion-decay is directly proportional to $n_i U_{\text{rel},i} V$, where

n_i is the number density of thermal ions, $U_{\text{rel},i} = \zeta_{\text{rel},i} U_{\text{th}}$ is the energy density of non-thermal ions, and V is the volume occupied by the WCR. Since $U_{\text{th}} \propto n_i \propto D^{-2}$, $U_{\text{rel},i} \propto \zeta_{\text{rel},i} D^{-2}$. In the adiabatic limit, the volume of the WCR scales as D^3 , so the intrinsic flux from neutral pion decay should scale as $\zeta_{\text{rel},i} D^{-1}$. As we do not know how (or if) $\zeta_{\text{rel},i}$ varies with D , the overall dependence on D is unknown. However, since the optical depth from two-photon pair production increases as D^{-1} , the observed flux above 100 GeV is likely to decline as D is reduced. An added complication is that γ_{\max} for the non-thermal ions will increase with decreasing D if the stars move sufficiently close that the geometry of the magnetic field in the unshocked stellar winds changes from toroidal to radial. In the radial limit, we expect that $\gamma_{\max} \propto 1/D$, and thus γ_{\max} may reach values of 10^6 in close systems (cf. Bednarek 2005). Table 4 summarizes the emission from the model components in various instrumental bands.

Fig. 18 also compares the non-thermal X-ray and γ -ray emission calculated from our model with the observed ASCA data at $\phi = 0.837$ - dataset 27022010, observed on 1999-10-22. The O star is in front of the WR star at this orbital phase, and although the IC emission will be slightly higher when a full treatment of the anisotropy of the scattering is accounted for, the increase should be less than a factor of 3 (see Fig. 10 in Reimer, Pohl & Reimer 2006). It is reassuring that even with this factored in, the model IC fluxes are significantly lower than the observed X-ray emission, consistent with the lack of detection of an underlying power-law component. The inset of Fig. 18 shows the intrinsic and attenuated thermal X-ray emission from model B. An important point is that the attenuated emission is in close agreement with the ASCA data. Unfortunately, this is also the case for our model A, and so the X-ray absorption at phase 0.837 cannot be used to constrain η .

Models of the radio data alone are ill-constrained (see Sec. 4.3), and the properties of their high energy non-thermal emission provides an important tool for discriminating between the models. In Fig. 19, the high-energy spectra of models A and B, are shown. The flux from model B is slightly higher than from model A because $\zeta_{\text{rel},e}$ and $\zeta_{\text{rel},i}$ are slightly higher, and the IC emission has a slightly steeper spectral slope in model B due to stronger IC cooling of the non-thermal electron energy spectrum resulting from the smaller distance between the apex of the WCR and the O star.

Fig. 20 shows the high energy non-thermal emission from models C, D, and E. The degeneracy of the emission at radio wavelengths is broken at high energies where clear differences in the models occur. In particular, the decrease in p from model C ($p = 1.53$) to model E ($p = 1.1$) is clearly manifest in the spectral slope, while the increase in $\zeta_{\text{rel},e}$ from model C to E is apparent in the relative normalization of the spectra. Since model E has $\zeta_{\text{rel},e} = 2.8 \times 10^{-2}$ which precludes setting $\zeta_{\text{rel},i} = 100\zeta_{\text{rel},e}$, we instead set $\zeta_{\text{rel},i} = 30\zeta_{\text{rel},e}$ for this model.

The high energy non-thermal emission from models B and F are compared in Fig. 21, where the main difference is in the assumed stellar luminosities. The spectral slope of the IC emission at energies greater than 0.1 MeV reflects the different values of p in these models. This emission arises predominantly from those electrons near the apex of the WCR

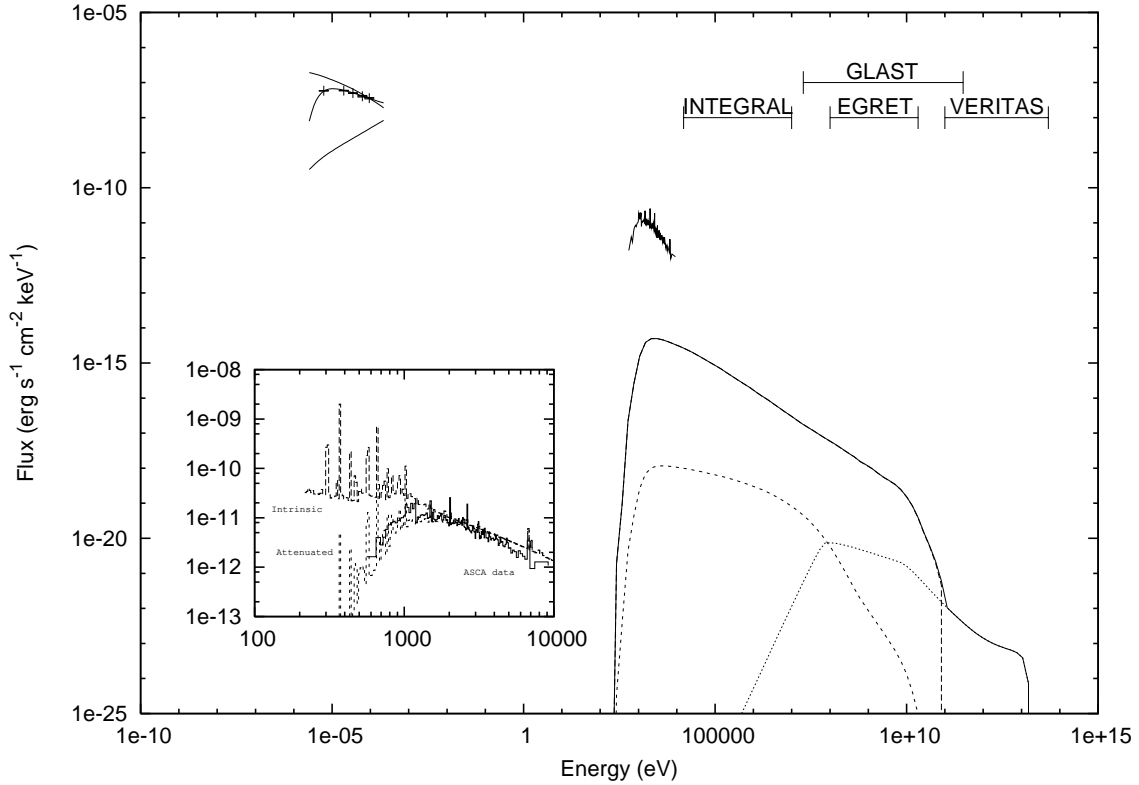


Figure 18. The radio, and non-thermal UV, X-ray and γ -ray emission calculated from model B, together with the observed radio and X-ray flux. The radio model shown indicates the thermal free-free flux (displayed below the data points), the *intrinsic* synchrotron flux before free-free absorption (displayed above the data points), and the total observed emission (cf. Fig. 10). The model IC (long dash), relativistic bremsstrahlung (short dash), and pion decay (dotted) emission components are shown, along with the total emission (solid). Photoelectric absorption is significant at soft X-ray energies up to ~ 2 keV. To calculate the IC and relativistic bremsstrahlung emission, $\zeta_{\text{rel},e} = 5.36 \times 10^{-3}$, as derived from the fit to the radio data (Fig. 10) was assumed. $\zeta_{\text{rel},i} = 100 \times \zeta_{\text{rel},e}$ was assumed to calculate the neutral pion decay emission. The observed *ASCA* X-ray spectrum from $\phi = 0.837$ is also shown. The intrinsic (dashed line) and attenuated (dotted line) thermal X-ray emission from model B is displayed in the inset, where we have assumed unmodified collisional shocks, rapid thermalization of the post-shock electrons, and collisional ionization equilibrium in our model. The ISM absorbing column was fixed at $N_{\text{H}} = 5.4 \times 10^{21} \text{ cm}^{-2}$ (Zhekov & Skinner 2000), and the absorption coefficients for the ISM and the WR and O star winds were calculated using Cloudy v94.00 (Van Hoof, Martin & Ferland 2000, see <http://www.nublado.org>).

Table 4. The high energy non-thermal emission from model B of WR 140 at orbital phase 0.837, with $\eta = 0.02$ and $\zeta_{\text{rel},e} = 5.36 \times 10^{-3}$. $\zeta_{\text{rel},i} = 100 \times \zeta_{\text{rel},e}$ is assumed for the calculation of the emission from neutral pion decay. The IC emission dominates the total emission in each energy band noted in this table.

Mechanism	Total emission (erg s^{-1})	EGRET (100MeV-10GeV) (erg s^{-1})	EGRET (100MeV-10GeV) ($\text{photons s}^{-1} \text{cm}^{-2}$)	INTEGRAL IBIS (15keV-10MeV) ($\text{photons s}^{-1} \text{cm}^{-2}$)	GLAST (20MeV-300GeV) ($\text{photons s}^{-1} \text{cm}^{-2}$)
Inverse Compton	3.5×10^{33}	2.1×10^{33}	5.4×10^{-9}	2.7×10^{-6}	1.5×10^{-8}
Rel. bremsstrahlung	1.8×10^{30}	3.2×10^{29}	2.5×10^{-12}	2.0×10^{-9}	2.1×10^{-11}
π^0 decay	6.8×10^{31}	9.8×10^{30}	1.3×10^{-11}	3.9×10^{-14}	1.8×10^{-11}

with initial post-shock Lorentz factors greater than ~ 100 . All such electrons rapidly cool to Lorentz factors of approximately 12 (model B) and 25 (model F) before advecting out of the system. Although the absorption of γ -rays by pair-production is lessened in model F due to the reduced stellar luminosities assumed, the commensurate reduction in $\zeta_{\text{rel},e}$ (and thus $\zeta_{\text{rel},i}$) and the increase in p lead to an overall decrease in the VERITAS flux (Table 5).

Fig. 22 shows a comparison between the high energy

non-thermal emission from models where free-free absorption (model B) or the Razin effect (models G, H, I and J) is responsible for the low frequency radio turnover. The large values of $\zeta_{\text{rel},e}$ in models G-J cause the IC flux to be at least two orders of magnitude higher relative to model B. Future observations with AGILE and GLAST should have the sensitivity to detect such fluxes, thus allowing a process of discrimination between our models. In fact, we can already exclude model G, since its predicted non-thermal

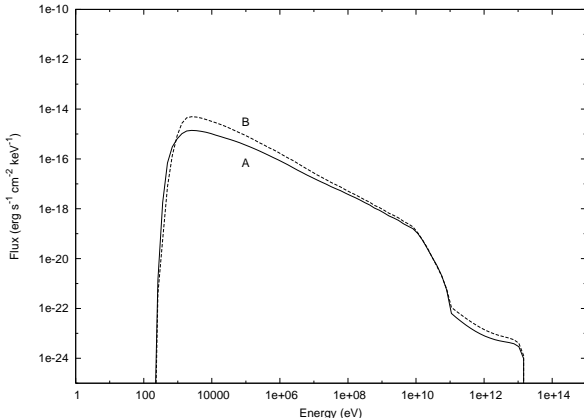


Figure 19. The high energy non-thermal emission calculated from models A and B with $p = 1.4$.

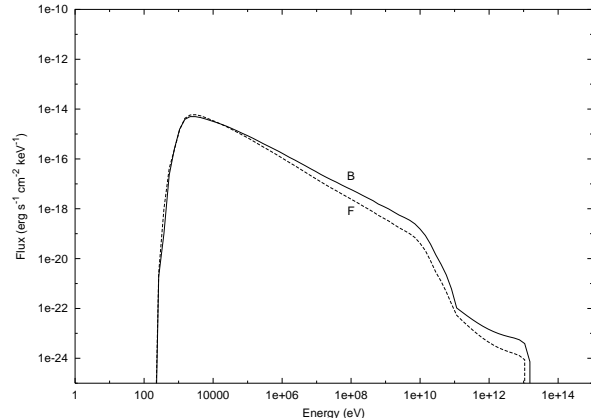


Figure 21. The high energy non-thermal emission calculated from models B and F, with $\eta = 0.02$.

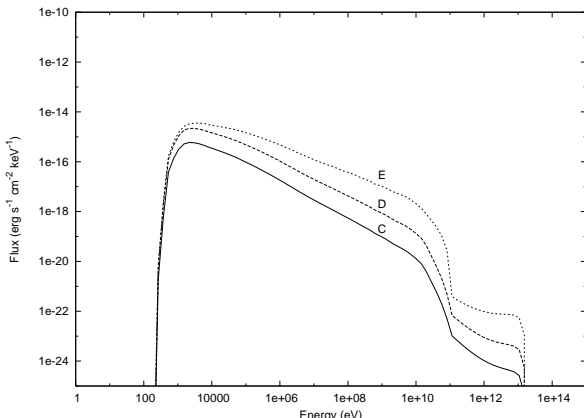


Figure 20. The high energy non-thermal emission calculated from models C, D and E, with $\eta = 0.11$.

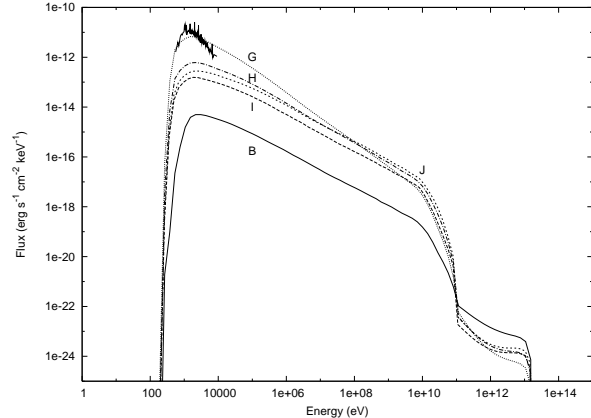


Figure 22. The high energy non-thermal emission calculated from models B, and G-J. The low frequency radio turnover in model B is due to free-free absorption, while in models G-J it is due to the Razin effect. The ASCA data are also shown.

emission exceeds the observed *thermal* emission at X-ray energies. While models H-J cannot be excluded in the same manner, there are other reasons why they are less desirable than model B (see Sec. 4.3.2). Table 5 notes the non-thermal luminosities and fluxes in various energy bands from each model.

4.4.2 Comparison to observations

The total photon flux in the EGRET band from models A-F (where free-free absorption is responsible for the low frequency radio turnover) varies from 4.8×10^{-10} photons $\text{s}^{-1} \text{cm}^{-2}$ (model C) to 4.2×10^{-8} photons $\text{s}^{-1} \text{cm}^{-2}$ (model E). The highest prediction is still below the flux detected from 3EG J2022+4317 during the December 1992 observation at $\phi = 0.97$ ($2.47 \pm 0.52 \times 10^{-7}$ photons $\text{s}^{-1} \text{cm}^{-2}$). While the different orbital phases of the radio and EGRET data prevent a direct comparison, the IC emission should increase between phase 0.837 and 0.97 as the stellar separation decreases by about a factor of three. Thus, the models with the highest predicted fluxes are broadly consistent with the data. In contrast, models G, H and J have predicted photon fluxes in the EGRET band

which exceed that observed from 3EG J2022+4317. This is an additional reason why these models are not as desirable as those where free-free absorption is responsible for the low frequency radio turnover.

In model B, the photon spectral index of the total non-thermal emission, Γ , is -2.9 at 1 keV (due to photoelectric absorption), 1.7 at 1 MeV and 100 MeV, 1.8 at 1 GeV, and 2.5 at 10 GeV, and is in rough agreement with the observed EGRET value of $\Gamma = 2.31 \pm 0.19$ between 100 MeV–10 GeV. Model E has the flattest non-thermal spectrum, with $\Gamma = -1.0$ at 1 keV, 1.55 at 1 MeV and 100 MeV, 1.6 at 1 GeV, and 2.1 at 10 GeV, and matches the observed spectral slope less well.

4.4.3 Comparison to previous work

The non-thermal γ -ray emission from WR 140 has previously been estimated by Benaglia & Romero (2003) and Reimer, Pohl & Reimer (2006). Since Benaglia & Romero's calculations are based on a stellar separation of 10 AU (corresponding to $\phi = 0.95$), neither our estimates, their estimates, or the EGRET detections, can be directly compared.

Table 5. The high energy non-thermal emission calculated from the models in Table 3.

Model	Total emission (erg s^{-1})	EGRET (100MeV-10GeV) (erg s^{-1})	EGRET (100MeV-10GeV) ($\text{photons s}^{-1} \text{cm}^{-2}$)	INTEGRAL IBIS (15keV-10MeV) ($\text{photons s}^{-1} \text{cm}^{-2}$)	GLAST (20MeV-300GeV) ($\text{photons s}^{-1} \text{cm}^{-2}$)	VERITAS (200GeV-50TeV) ($\text{photons s}^{-1} \text{cm}^{-2}$)
A	2.4×10^{33}	1.5×10^{33}	3.4×10^{-9}	1.0×10^{-6}	1.0×10^{-8}	2.7×10^{-14}
B	3.6×10^{33}	2.1×10^{33}	5.4×10^{-9}	2.7×10^{-6}	1.5×10^{-8}	4.5×10^{-14}
C	3.2×10^{32}	1.8×10^{32}	4.8×10^{-10}	3.0×10^{-7}	1.4×10^{-9}	3.5×10^{-15}
D	2.8×10^{33}	1.6×10^{33}	4.0×10^{-9}	1.5×10^{-6}	1.1×10^{-8}	2.8×10^{-14}
E	3.6×10^{34}	2.0×10^{34}	4.2×10^{-8}	4.2×10^{-6}	9.4×10^{-8}	2.8×10^{-13}
F	1.3×10^{33}	7.0×10^{32}	2.0×10^{-9}	2.4×10^{-6}	6.3×10^{-9}	1.5×10^{-14}
G	2.4×10^{35}	7.6×10^{34}	2.8×10^{-7}	1.4×10^{-3}	1.1×10^{-6}	8.0×10^{-15}
H	1.9×10^{35}	1.1×10^{35}	3.1×10^{-7}	2.7×10^{-4}	9.5×10^{-7}	9.9×10^{-15}
I	1.1×10^{35}	6.8×10^{34}	1.7×10^{-7}	8.1×10^{-5}	4.7×10^{-7}	6.5×10^{-15}
J	2.4×10^{35}	1.5×10^{35}	4.0×10^{-7}	1.7×10^{-4}	1.1×10^{-6}	1.1×10^{-14}

Their estimate for the IC luminosity in the EGRET band of $2.1 \times 10^{34} \text{ erg s}^{-1}$ is typically higher than the values from our models A-F, but lower than those from models G-J (cf. Table 5).

There are substantial differences between this work and that of Benaglia & Romero (2003): their estimate is obtained through the use of Eq. 3, in which the ratio of the IC to synchrotron emission depends strongly on the B-field, and is based on only a single position in the WCR. They estimate that $B = 200 \text{ mG}$ (although noting its value is quite uncertain). In contrast, here the IC emission is determined from models of the radio emission. The magnetic field is a fitted (though ill-constrained) parameter of the models, with a maximum at the stagnation point³, and rapidly declines in the downstream flow. Also, in the approach presented here the B-field directly affects the synchrotron emission, but also indirectly affects the calculations of the high energy emission which depend on the population and spatial distribution of non-thermal particles i.e. $\zeta_{\text{rel,e}}$ and $\zeta_{\text{rel,i}}$. Finally, Benaglia & Romero (2003) use the *observed* synchrotron luminosity, rather than the intrinsic luminosity, leading to an underestimate of the IC luminosity.

Our estimates for the relativistic bremsstrahlung luminosity are broadly consistent with the limit of $< 10^{32} \text{ erg s}^{-1}$ noted in Benaglia & Romero (2003), but the pion decay luminosities are wildly discrepant with our lowest estimate being 10 orders of magnitude higher. Details of their calculation are noted in Benaglia et al. (2001), where a ‘‘cosmic ray enhancement factor’’ of 10 is assumed. This factor is the ratio between the cosmic ray energy density at the source (in this case the WCR) and that observed at the Earth (which is roughly equal to the average cosmic ray energy density within the Galaxy of $\approx 1 \text{ eV cm}^{-3} = 1.6 \times 10^{-12} \text{ erg cm}^{-3}$). However, at the head of the WCR, the energy density of relativistic ions in our model B, for example, is $\approx 0.64 \text{ erg cm}^{-3}$. This corresponds to a cosmic ray enhancement factor of $\sim 10^{11}$, and accounts for the large underestimate of the pion decay emission by Benaglia & Romero (2003).

³ Since the magnetic field is not well constrained by the radio fits, there is a large variation in its strength between models. For instance, at the apex of the WCR, $B = 74 \text{ mG}$ in model G, rising to 3.3 G in model C, and is 1.2 G in our preferred model (B).

Reimer, Pohl & Reimer (2006) have also calculated the expected high energy non-thermal flux from WR 140. They conclude that the change in the IC flux with viewing angle due to anisotropic scattering is likely to be obscured by large variations in the energy density of the stellar radiation fields resulting from the high orbital eccentricity. While anisotropic IC emission and Klein-Nishina effects are clearly processes which should be included in future models, our work shows that other uncertainties, such as the value of p , currently have a greater influence on the IC emission.

4.4.4 Predictions for forthcoming instruments

Our predictions for the flux in the energy band of the IBIS instrument onboard INTEGRAL and the GLAST large area telescope (LAT) are also noted in Table 5. For models A-F the predicted fluxes are $\sim 10^3 \times$ lower in the INTEGRAL band, and $\sim 10^2 \times$ lower in the GLAST band than those made by Benaglia & Romero (2003). Using the INTEGRAL Observing Time Estimator⁴, we find that model A cannot be detected at the 5σ level in the $15 \text{ keV} - 10 \text{ MeV}$ range using the IBIS imager, since an exposure time of 300 yrs is required! Model E, the brightest of models A-F in this band, still requires an exposure of 180 yrs. With several bright sources (including Cyg X-1) nearby, the required exposure time may be even longer. On the other hand, for model J an exposure time of only 2.8 Msec is needed. At the time of writing, WR 140 is not detected in a 2 Msec exposure (De Becker 2005), and we are close to ruling out model J (and H) on this basis. Line emission at γ -ray energies from the de-excitation of nuclear isomers, such as $^{12}\text{C}^*$ and $^{16}\text{O}^*$, is much too faint to be detected with current instrumentation (Benaglia & Romero 2003).

The GLAST 5σ sensitivity at $E > 100 \text{ MeV}$ for sources at high galactic latitudes with a $\Gamma = 2$ spectrum after a 2 yr all-sky survey is $1.6 \times 10^{-9} \text{ photons s}^{-1} \text{cm}^{-2}$. Therefore, our predictions suggest that WR 140 will be detectable, this being important to differentiate between the models in Table 5.

At energies of approximately 50 GeV and higher, the flux from the models arises exclusively from the decay of

⁴ <http://integral.esac.esa.int/isoc/operations/html/OTE.html>

neutral pions, with a high energy cut off of ≈ 15 TeV, strongly dependent on γ_{\max} of the ions. The VERITAS-4 array is sensitive to γ -rays in the 200 GeV to 50 TeV energy band, but unfortunately the high absorption from two-photon pair production severely reduces the photon flux above ~ 10 GeV. The predicted flux from model B is not sufficient for a detection in a 50 hr observation (cf. Fegan, Hall & Vassiliev 2003), and we conclude that WR 140 is probably too faint to be detected at $\phi = 0.837$, though it might be brighter at phases closer to periastron. An observation by GLAST, for example, will better constrain the potential models, and allow more robust predictions of the flux at \sim TeV energies.

5 DISCUSSION

5.1 Mass-loss rates of early-type stars

It is important that accurate measurements of mass-loss rates from early-type stars are obtained, as mass-loss is known to significantly affect their evolution, and the injection of mass, momentum and energy influences not only the gas-phase conditions in the immediate environment of the clusters within which the massive stars form, but also the phase structure and energetics of the ISM on galactic scales, and the thermodynamics and enrichment of the intergalactic medium on Mpc scales and above.

Unfortunately, observational determinations of mass-loss rates are often highly uncertain, in part because many of the techniques are sensitive to the degree of structure in the winds. Overestimates by factors of at least 3 or more are likely when the winds are clumpy, but for some types of O stars it could be as high as factors of 20 or more (Fullerton, Massa & Prinja 2006). The X-ray emission from CWB systems provides an opportunity to measure mass-loss rates using a method which is not expected to be very sensitive to clumping (see Sec. 4.2.3). In fact, mass-loss rates could be underestimated using this technique: at least some winds may be both denser and faster at high latitudes (Dwarkadas & Owocki 2002; Smith 2002; Chesneau et al. 2005), and if the stellar rotation axes of the stars are closely perpendicular to the orbital plane, the WCR then probes those parts of the winds which are less dense and slower. In addition, a significant amount of energy may be siphoned into particle acceleration. In this work, the mass-loss rate for the O supergiant star in WR 140 is towards the lower end of previous estimates, but is consistent with expected biases. A reduction in mass-loss rates, and/or mass-loss through a predominantly polar flow, can also explain the near-symmetry of observed X-ray lines from early-type stars (Owocki & Cohen 2006; Mullan & Waldron 2006; Cohen et al. 2006), and both reduced mass-loss and polar flow help in the theoretical formation of gamma-ray bursts (Woosley & Heger 2006).

5.2 The nature of shocks and particle acceleration in wide CWB systems

In this work we have presented evidence for a fairly hard spectrum (i.e. $p < 2$) of non-thermal electrons in WR 140, which is further supported by earlier fits to the radio data

of WR 147 (this was mistakenly interpreted as evidence for shock modification in Pittard et al. 2006). As discussed in Sec. 2.1.3, there are many potential mechanisms for producing $p < 2$. One possibility is particle re-acceleration, but while the wind-embedded shocks believed to occur in stellar winds due to the line de-shadowing instability of the radiative driving (e.g., Owocki, Castor & Rybicki 1988) may provide such an opportunity, and thus harden the non-thermal particle spectrum prior to the global shocks bounding the WCR, further evidence is needed for this explanation to be more persuasive, not least because re-acceleration has yet to be demonstrated in theoretical calculations of wind-embedded shocks. One problem is that in current one-dimensional simulations of wind-embedded shocks, the accelerated particles are trapped between forward and reverse shocks. This has posed a problem for the interpretation of non-thermal radio emission from single stars (Van Loo, Runacres & Blomme 2006), and only calculations using a phenomenological shock model are currently successful in fitting the data (e.g., Chen & White 1994). Two- and three-dimensional models of instability-generated structure (see, e.g., Dessart & Owocki 2003) may allow accelerated particles to escape one shock and be re-accelerated at others, but this has still to be demonstrated.

We can speculate about additional effects which occur in CWB systems with highly eccentric orbits. For example, if re-acceleration is important, one might expect p to depend on the orbital phase, as the number of wind-embedded shocks that accelerate a non-thermal particle prior to the WCR may change significantly as the stellar separation alters. Similarly, if the obliquity of the shocks changes with stellar separation, the injection efficiency and rate of particle acceleration may also alter. In addition, it is likely that the maximum energy obtained by electrons and ions varies with stellar separation. Finally, the assumption of isotropic synchrotron emission will need to be reconsidered if the magnetic turbulence is low enough that the mean B-field has a preferred direction. In the context of WR 140, these are all potential explanations for the observed asymmetry of the radio lightcurve.

Is the efficiency of particle acceleration in WR 140 high enough for shock modification to occur? In Tycho's SNR, the concave curvature of synchrotron radio emission is clear, though still indirect, evidence for shock modification (see Volk et al. 2002). Unfortunately, in WR 140 the observed synchrotron emission extends over a much narrower frequency range and a concave curvature cannot easily be distinguished. And while the lower than expected thermal X-ray temperature is consistent with shock modification, a more probable cause is $T_e < T_i$. Likewise, while shock modification may help to explain the behaviour of the X-ray lightcurve which does not follow the expected $1/D$ variation for an adiabatic WCR (Pollock, Corcoran & Stevens 2002), there is a realistic chance that radiative cooling is the cause. Finally, the B-field in WR 140 is sufficiently high to cause significant energy to be transferred from the non-thermal particles into magnetic turbulence via Alfvén wave heating, thereby lowering the acceleration efficiency, although it remains possible that shock modification occurs predominantly through particle loss (due to the curvature of the shocks) rather than high acceleration efficiencies. To summarize, there is currently no strong evidence for shock modifi-

cation in WR 140, and on balance we conclude that strongly modified shocks are unlikely to occur in WR 140.

5.3 Non-thermal X-ray, TeV and muon neutrino emission from CWBs

While there is no observational evidence for non-thermal X-ray emission in WR 140, there are some systems that appear to show a power-law tail. Perhaps the strongest candidate is η Carinae, where X-rays with a photon index $\Lambda \approx 2.4$ were detected at energies of up to 150 keV during a long BeppoSAX exposure (Viotti et al. 2004). Determining the spectral slope at higher energies should allow discrimination of the competing models proposed to explain this emission.

The lack of observed non-thermal X-ray emission from CWB systems which are known non-thermal radio emitters (De Becker et al. 2004a, 2005, 2006) contrasts with the possible detection of non-thermal X-ray emission from the 3.4 d orbital period system HD 159176, which is not known to be a non-thermal radio emitter (De Becker et al. 2004b). Though the nature of the wind-wind collision in such short period systems is uncertain, if particle acceleration occurs, perhaps mainly through reconnection, IC losses will be catastrophic, and it is not surprising that non-thermal X-ray emission is possibly detected despite no clear signature of synchrotron emission (due to the obvious high absorption - De Becker 2005).

In the models of WR 140 presented in this paper, absorption of high energy photons by pair-production creates a very steep photon spectrum between 10 GeV and 1 TeV. Consequently, the photon flux above 1 TeV is many times lower than the flux predicted in the VERITAS bandpass, which is dominated by photons with energies less than 1 TeV (see Table 5). For example, in model B the flux above 1 TeV is 1.2×10^{-14} photons $\text{s}^{-1} \text{cm}^{-2}$. Nevertheless, the flux from CWB systems compares favourably to some other mechanisms proposed for the generation of TeV emission, such as the interaction of cosmic rays in the innermost parts of the winds of early-type stars (Torres, Domingo-Santamaría & Romero 2004) or within the cluster wind of a dense stellar cluster (Domingo-Santamaría & Torres 2006). Therefore, it is possible that several CWBs or multiple colliding winds from a cluster of stars contribute part or all of the flux from the unidentified TeV source detected in the Cygnus region, TeV J2032+4130 (Aharonian et al. 2005a), which has an integral flux $F_\gamma(E_\gamma > 1 \text{ TeV}) = 6.9(\pm 1.8) \times 10^{-13}$ photons $\text{s}^{-1} \text{cm}^{-2}$. The unidentified TeV source HESS J1813-178 (with an integrated flux above 200 GeV of 1.2×10^{-12} photons $\text{s}^{-1} \text{cm}^{-2}$) may also be associated with an OB association (Aharonian et al. 2005b).

The decay of charged pions created in hadronic collisions between non-thermal and thermal ions produces a $\nu_\mu + \bar{\nu}_\mu$ neutrino flux. This flux can be estimated from the γ -ray flux produced by neutral pion-decay by imposing energy conservation (Alvarez-Muñiz & Halzen 2002). Fig. 23 shows the resulting flux from models B and E, including neutrino oscillation. It is clear that the predicted fluxes are neither above the atmospheric neutrino background (ANB), nor above the sensitivity limit of the proposed IceCube detector. Thus, our finding is contrary to the conclusion of Bednarek (2005), who predicted a detectable muon neutrino

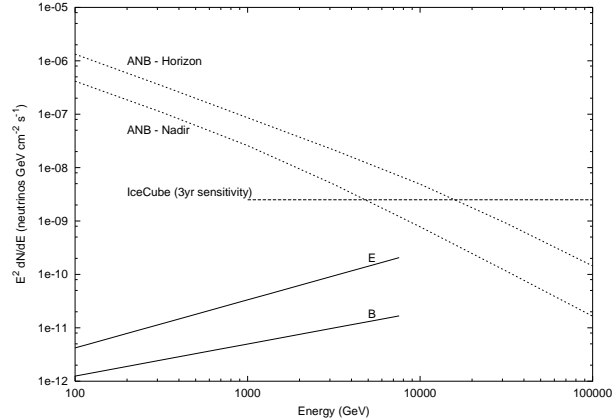


Figure 23. The differential spectra of muon neutrinos produced by neutral pion decay from models B and E (the fluxes have been reduced by a factor of 2 to account for neutrino oscillation). The atmospheric neutrino background flux within 1° of the source (Lipari 1993) is shown, together with the 3-yr sensitivity of the IceCube detector (Hill 2001).

flux from WR 20a. This discrepancy is due to Bednarek's use of a higher conversion efficiency of kinetic power into non-thermal particles, largely through the assumption $\eta = 1$.

5.4 Colliding winds in dense stellar clusters

Our work is also relevant to more complicated systems involving colliding winds, such as dense stellar clusters. Hydrodynamical simulations of the multiple colliding winds in clusters have been performed by Raga et al. (2001), with particular application to the Galactic Center in Coker & Melia (1997), Coker & Pittard (2005), Rockefeller et al. (2005), and Cuadra et al. (2006). A network of bubbles forms around the stars, which are embedded in a medium of hot shocked gas. Highly non-linear DSA should occur at the stellar termination shocks in stellar clusters if the pre-shock B-field is small enough ($B \lesssim 10 \mu\text{G}$, Ellison, Decourchelle & Ballet 2005), though the most extreme modification (e.g., compression ratios much greater than 4) will occur only at the cluster's edge.

Shock modification is also a potential explanation for the lower than expected temperature of the X-ray emitting gas observed in several dense stellar clusters (e.g., Stevens & Hartwell 2003), though mass-loading and slow equilibration of the post-shock ion and electron temperatures are other possibilities. In addition, the X-ray luminosities of the diffuse gas are generally higher than expected, which indicates mass-loading and/or a low thermalization efficiency (Stevens & Hartwell 2003; Oskinova 2005), the latter also being consistent with efficient particle acceleration and shock modification. If the rate at which energy is removed from the cluster (for example, by radiative cooling) exceeds 30% of the energy injection rate, a time independent cluster wind cannot form (Silich, Tenorio-Tagle & Rodríguez-González 2004). Though the removal of energy through particle acceleration was not considered, efficiencies of this order are expected (e.g., Bykov 1999), in which case a full time-dependent solution for the cluster wind is required.

Amongst the dense stellar clusters known in our Galaxy, the central cluster around Sgr A* is unusual in many respects, including the recent detection of apparently thermal gas with a temperature $kT \approx 8$ keV (Muno et al. 2004), and TeV emission. Observations with HESS show a 1-10 TeV luminosity of $\sim 10^{35}$ erg s $^{-1}$ (Aharonian et al. 2004). The upper limit on the TeV source size is $< 3''$ (95% confidence level), which corresponds to < 7 pc at the distance of the Galactic Center. The photon spectrum above the 165 GeV threshold is specified by $F(E) = F_0 E_{\text{TeV}}^{-\Gamma}$, with $\Gamma \approx 2.2$ and $F_0 \approx 2.5 \times 10^{-12}$ photon s $^{-1}$ cm $^{-2}$ TeV $^{-1}$, and has been independently confirmed with MAGIC (Albert et al. 2006). Various origins of the TeV emission have been proposed, including the central supermassive black hole (Aharonian & Neronov 2005a), the young SNR Sgr A East (Crocker et al. 2005), the dark matter halo (Horns 2005), and from non-thermal particles accelerated at the multiple colliding winds shocks (Quataert & Loeb 2005), which we now discuss.

The total wind power estimated from the cluster of stars within $\sim 10''$ (~ 0.4 pc) of the Galactic Center is $\sim 3 \times 10^{38}$ erg s $^{-1}$. In the context of colliding winds, the TeV emission may arise from IC upscattering of ambient photons by non-thermal electrons, or from the decay of neutral pions created by the collisions of non-thermal and thermal hadrons. We now consider each process in turn. It is likely that IC cooling limits the maximum Lorentz factor that non-thermal electrons within the central parsec can attain to $\sim 10^7$ (Quataert & Loeb 2005), which is only marginally high enough for IC scattering to account for the detected TeV flux. The TeV emission occurs from electrons whose cooling time is less than the flow time out of the cluster i.e. from those with $\gamma > \gamma_c$. For a power-law distribution of electrons $n(\gamma) \propto \gamma^{-p}$, the IC photon spectral index is $\Gamma = (p + 2)/2$, for $\gamma > \gamma_c$. Hence the TeV spectral index of 2.2 implies that $p \approx 2.4$. If instead neutral pions are responsible, the observed spectral index indicates that $p \approx 2.2$. In the context of multiple colliding winds, Ozeroy, Genzel & Usov (1997) estimates the emission from pion-decay to be $\sim 3 \times 10^{36}$ erg s $^{-1}$, assuming 10% acceleration efficiency for hadrons at the multiple shocks, and a 10% energy transfer into pions i.e. a 1% efficiency overall. Other estimates in the literature suggest a somewhat lower luminosity from this process (e.g., Quataert & Loeb 2005), but this process nevertheless appears to be plausible on energy grounds.

The required value of p for each of these processes is much softer than we find here for WR 140, and also for the theoretical limit for multiple shocks ($p=1.0$, Pope & Melrose 1994). This implies that re-acceleration at multiple shocks within the cluster, as proposed by Ozeroy, Genzel & Usov (1997), does not occur. It is possible to imagine several reasons why this might be the case. Firstly, there is unlikely to be a seed population of non-thermal particles from wind-embedded shocks encountering the termination shock of the winds because of the large adiabatic cooling experienced as the plasma flows out to $\sim 0.01 - 0.1$ pc. Hence, the particle spectrum immediately downstream of the termination shocks is likely to correspond to the single-shock limit. Secondly, it is not entirely clear that there will be numerous opportunities for particle re-acceleration within the radius of the cluster, since the cooling timescale of the shocked gas

is long, and it remains hot, and therefore subsonic. Analytical solutions of cluster winds reveal that the shocked gas, on average, only becomes supersonic at the outer radius of the cluster (Chevalier & Clegg 1985). Within the cluster interior, the network of hot post-shock gas experiences pressure gradients and weak shocks as it escapes, but in general is not likely to be repeatedly shocked. This lack of opportunity for re-acceleration means that p is likely to remain close to the value obtained from a single shock.

Perhaps the most natural explanation is that the majority of particle acceleration occurs at low Mach number shocks ($M \approx 3$ and $M \approx 5$, for IC or pion-decay emission respectively) within the network of hot shocked gas. This conclusion does not rule out the possibility of modification at the termination shocks of the individual winds, which would be consistent with the low X-ray temperature of the cooler emission component ($kT \approx 0.8$ keV, Muno et al. 2004), but does exclude shock modification as the only process since a hard particle spectrum ($p < 2$) is expected at the high particle energies ($\gamma \gtrsim 10^5$) which are necessary. An alternative explanation is sub-diffusive cross-field transport (see Sec. 2.1.3).

The Galactic Center region has also been detected at GeV energies. The observed luminosity of the EGRET source 3EG J1745-2852 is $\approx 2 \times 10^{37}$ erg s $^{-1}$ (Mayer-Hasselwander et al. 1998; Hartman et al. 1999). However, while its position is consistent with Sgr A*, the angular resolution of 1° covers a solid angle about 100 times larger than the emission seen with HESS. As the EGRET spectrum is about 4 orders of magnitude brighter than the observed HESS emission extrapolated as a power-law to GeV energies, different processes/sources may well be responsible for the detected emission (although different assumptions concerning the injection spectrum and diffusion coefficients of non-thermal protons may account for both observations, as shown by Aharonian & Neronov 2005b). Regardless of the origin of non-thermal protons, if the emission is from pion-decay, a substantial TeV neutrino flux should be seen by neutrino telescopes.

While it remains difficult to draw firm conclusions on the nature of the TeV emission observed from the Galactic Center, we note that the nearby Arches cluster, which has an integrated mass-loss rate from its stellar components within an order of magnitude of the Galactic Center cluster, has not yet been detected at TeV energies. This may argue against the cluster wind scenario as an explanation for the TeV emission from the Galactic Center.

6 SUMMARY AND FUTURE DIRECTIONS

In this paper we have applied models to the observed emission from WR 140 at $\phi = 0.837$, when the radio emission is near maximum, and when X-ray data are available. Predictions for the X-ray and γ -ray emission from IC scattering, relativistic bremsstrahlung, and neutral pion decay, as well as for the muon neutrino flux, are made. Our calculations are based on the orbital solution of Dougherty et al. (2005), and contain a number of simplifying assumptions, including i) that the non-thermal electrons and ions are accelerated at the shocks bounding the WCR (this is assumed to be through DSA, but need not necessarily be so) and have

power-law spectra with a sharp cutoff at $\gamma_{\max} = 10^5$ before advecting downstream, ii) the non-thermal particle distribution at these shocks is normalized with respect to the local post-shock thermal energy density, the non-thermal ions have $100\times$ the energy density of the non-thermal electrons, and neither the spectral index of the energy distribution nor γ_{\max} vary along the shocks, iii) the energy density of the magnetic field is similarly normalized to the local post-shock thermal energy density, iv) particle acceleration has no effect on the thermal shock structure i.e. there is no shock “modification”, v) IC cooling occurs in the Thomson limit with isotropic scattering, vi) the emission from secondary particles is ignored. Rapid IC cooling of the high energy electrons in the post-shock flow means that the local value of γ_{\max} is typically $<< 10^5$. The assumptions $\gamma_{\max} = 10^5$ and $\zeta_{\text{rel},i} = 100\zeta_{\text{rel},e}$, together with the assumptions in v), mean that the predicted emission at GeV energies and above is relatively uncertain at this stage. Our predictions for the VERITAS-4 flux, in particular, should be treated as an estimate.

Despite the large number of assumptions listed above, it is possible to make a number of key deductions concerning the nature of WR 140 and the particle acceleration process at the WCR. We clearly show that VLBA imaging observations of WR 140 do not currently have enough sensitivity to constrain the wind momentum ratio η , through determination of the shock opening angle. VLBI observations are only sensitive to high-brightness emission that arises in the region of the apex of the WCR, where the WCR has yet to attain an asymptotic opening angle. Furthermore, we find that the relative positions of the stars and the peak of the observed emission from the WCR is not necessarily related to η , due to occultation by the stellar winds. Such observations have been used to determine η in a number of wider CWB systems where occultation effects are expected to be relatively unimportant (e.g. Dougherty et al. 1996; Dougherty, Williams & Pollacco 2000; Contreras et al. 1997; Williams et al. 1997), but we caution against the application of this method to closer systems like WR 140. In spite of these limitations in interpreting VLBA observations, it is possible to constrain the wind momentum ratio using simultaneous fits to the radio and X-ray data to $\eta \approx 0.02$. A remaining concern is that the line-of-sight angle into the system in our preferred model is some way from the observationally determined value, although the uncertainty in the latter is not negligible. Additional data is required to further constrain the orbital parameters of WR 140.

The stellar mass-loss rates in our preferred model are $\dot{M}_{\text{WR}} \approx 4.3 \times 10^{-5} \text{ M}_{\odot} \text{ yr}^{-1}$ and $\dot{M}_{\text{O}} \approx 8 \times 10^{-7} \text{ M}_{\odot} \text{ yr}^{-1}$. While the O star mass-loss rate is substantially lower than the values estimated by Repolust et al. (2004) for O4-5 supergiants, an order of magnitude reduction in the mass-loss rate is consistent with the recent estimates of Fullerton, Massa & Prinja (2006), and with some current explanations of the observed near-symmetry of X-ray lines. Such sizeable reductions have extensive implications for massive star evolution (including gamma-ray bursts), and feedback on the interstellar medium. There is also some scope for reducing the stellar luminosities adopted from Dougherty et al. (2005).

An important finding is that models of the radio data re-

quire $p < 2$. Several possible mechanisms can in principle explain this. In any case, a flatter spectrum for the non-thermal particles has important implications for the modelling of the high energy non-thermal emission from such systems, with almost all previous models in the literature assuming that $p = 2$. While our fits are currently non-unique, models where the Razin effect is responsible for the low frequency radio turnover (which allow $p = 2$) can be ruled out on the basis that the implied efficiency of electron acceleration is extraordinarily high. Furthermore, they predict the detection of IC emission by INTEGRAL which has not yet been achieved, and in some cases non-thermal X-ray emission at fluxes higher than the observed thermal emission. Observations with Suzaku should be more sensitive than those made with INTEGRAL, and will allow tighter constraints to be placed on the strength of the magnetic field. Our inability to obtain fits to the radio data with $p > 2$ does not necessarily exclude the possibility of shock modification, but on balance we believe that this is unlikely to occur in WR 140. However, large non-linear effects, comparable to those possible at the reverse shock in SNRs (Ellison, Decourchelle & Ballet 2005), may occur at the wind-wind collisions in stellar clusters where the B-field is much lower.

Our flux predictions at orbital phase 0.837 are summarized in Table 5. The photon fluxes in the INTEGRAL, GLAST, and VERITAS-4 band-passes range from $3 \times 10^{-7} - 3 \times 10^{-4}$, $10^{-9} - 10^{-6}$, and $4 \times 10^{-15} - 3 \times 10^{-13}$, respectively, with our preferred model having fluxes of 3×10^{-6} , 2×10^{-8} , and $5 \times 10^{-14} \text{ photons s}^{-1} \text{ cm}^{-2}$. The high energy non-thermal emission from WR 140 is expected to display significant variability with orbital phase as the stellar separation and line-of-sight angle change, both of which affect the opacity of absorption in the stellar radiation fields and the emission from the resulting IC cascade of secondary electrons and positrons. In addition, the spectral index and the acceleration efficiency of the primary non-thermal particles may also change. We emphasize that the future detection of TeV emission from CWB systems will almost certainly indicate pion-decay, since the high photon fluxes prevent the acceleration of electrons beyond $\gamma \sim 10^5 - 10^6$. WR 140, along with WR 146 which has the brightest non-thermal radio emission of any CWB (Dougherty, Williams & Pollacco 2000), and WR 147 which is the widest CWB system on the sky (Williams et al. 1997) and the only system resolved in X-rays (Pittard et al. 2002), present a real opportunity for the unambiguous detection of pion-decay from accelerated ions. The estimated flux of TeV photons from CWB systems compares favourably to some other mechanisms, and may contribute part or all of the flux from some TeV sources. The multiple colliding winds in the Galactic Center cluster may make a non-negligible contribution to the observed TeV flux. However, wide CWB systems are not expected to be strong neutrino sources.

Tighter constraints on p and the nature of the shocks and particle acceleration in colliding winds systems (binaries and clusters) are best achieved through the dual strategy of improving the theoretical models and obtaining observational data at MeV and GeV energies. On the theoretical side, models should explicitly account for the transfer of part of the available pre-shock energy into accelerated particles, self-consistently calculate the non-thermal electron and ion spectra and their subsequent evolution as they advect with

the downstream flow, and include Klein-Nishina effects and anisotropic IC scattering. Upcoming observations by AGILE and GLAST at MeV and GeV energies, where the emission is no longer degenerate with B and p , should then distinguish between the non-unique model fits to the radio data, and determine the B-field in the WCR and the spectral index of the non-thermal particles.

ACKNOWLEDGEMENTS

We have had many interesting discussions during the course of this work, and would like to thank Felix Aharonian, Paula Benaglia, Andrei Bykov, Paul Crowther, Chuck Dermer, Jamie Holder, Jim MacDonald, Anita Reimer, Sven van Loo, and Perry Williams. We would also like to thank Mike Corcoran for supplying the ASCA X-ray spectrum of WR 140, Rob Coker for comments on an earlier draft, and Evan O'Connor for running some early models. Johannes Knapp, Andy Pollock, Ian Stevens, and Perry Williams provided helpful comments prior to submission. Special thanks go to Don Ellison for his tireless response to questions over the course of the last few years. We would like to thank the referee for a constructive, timely, and helpful report. SMD gratefully acknowledges partial funding for a visit to Leeds. JMP is supported by a University Research Fellowship from the Royal Society. This research has made use of NASA's Astrophysics Data System Abstract Service.

REFERENCES

Aharonian F. A., Atoyan A. M., 1996, *A&A*, 309, 917
 Aharonian F. A., et al. (HESS collaboration), 2004, *A&A*, 425, L13
 Aharonian F. A., et al. (HEGRA collaboration), 2005a, *A&A*, 431, 197
 Aharonian F. A., et al. (HESS collaboration), 2005b, *Science*, 307, 1938
 Aharonian F. A., Neronov A., 2005a, *ApJ*, 619, 306
 Aharonian F. A., Neronov A., 2005b, *Astr. Space Sci.*, 300, 255
 Albert J., et al. (MAGIC collaboration), 2006, *ApJ*, 638, L101
 Alvarez-Muñiz J., Halzen F., 2002, *ApJ*, 576, L33
 Bamba A., Yamazaki R., Ueno M., Koyama K., 2003, *ApJ*, 589, 827
 Baring M. G., Harding A. K., 1997, *ApJ*, 491, 663
 Baring M. G., Ellison D. C., Reynolds S. P., Grenier I. A., Goret P., 1999, *ApJ*, 513, 311
 Bednarek W., 2005, *MNRAS*, 363, L46
 Bednarek W., 2006, *MNRAS*, 368, 579
 Bell A. R., 1978, *MNRAS*, 182, 147
 Bell A. R., 2004, *MNRAS*, 353, 550
 Benaglia P., Romero G. E., Stevens I. R., Torres D. F., 2001, *A&A*, 366, 605
 Benaglia P., Romero G. E., 2003, *A&A*, 399, 1121
 Berezhko E. G., Ksenofontov L. T., Völk H. J., 2003, *A&A*, 412, L11
 Berezhko E. G., Völk H. J., 2004, *A&A*, 419, L27
 Berrington R. C., Dermer C. D., 2003, *ApJ*, 594, 709
 Blumenthal G. R., Gould R. J., 1970, *Rev. Mod. Phys.*, 42, 237
 Bykov A. M., 1999, in *ASP Conf. Ser.* 171, LiBeB Cosmic Rays and Related X- and Gamma-Rays, eds. R. Ramaty, E. Vangioni-Flam, M. Cassé & K. Olive (San Francisco: ASP), 146
 Bykov A. M., Toptygin I. N., 2001, *Ast. Lett.*, 27, 735
 Chen W., White R. L., 1994, *ApJ*, *Ap&SS*, 221, 259
 Chesneau O., et al., 2005, *A&A*, 435, 1061
 Chevalier R. A., Clegg A. W., 1985, *Nature*, 317, 44
 Cohen D. H., Leutenegger M. A., Grizzard K. T., Reed C. L., Kramer R. B., Owocki S. P., 2006, *MNRAS*, 368, 1905
 Coker R. F., Melia F., 1997, *ApJ*, 488, L149
 Coker R. F., Pittard J. M., 2005, in *X-Ray and Radio Connections*, eds. L. O. Sjouwerman and K. K. Dyer, published electronically by NRAO, <http://www.aoc.nrao.edu/events/xrayradio>
 Contreras, M. E., Rodríguez, L. F., Tapia M., Cardini D., Emanuele A., Badiali M., Persi P., 1997, *ApJ*, 488, L153
 Crocker R. M., Fatuzzo M., Jokipii J. R., Melia F., Volkas R. R., 2005, *ApJ*, 622, 892
 Crowther P. A., Hillier D. J., Evans C. J., Fullerton A. W., De Marco O., Willis A. J., 2002, *ApJ*, 579, 774
 Cuadra J., Nayakshin S., Springel V., Di Matteo T., 2006, *MNRAS*, 366, 358
 De Becker M., Rauw G., Blomme R., Waldron W. L., Sana H., Pittard J. M., Eenens P., Stevens I. R., Runacres M. C., Van Loo S., Pollock A. M. T., 2004a, *A&A*, 420, 1061
 De Becker M., Rauw G., Pittard J. M., Antokhin I. I., Stevens I. R., Gosset E., Owocki S. P., 2004b, *A&A*, 416, 221
 De Becker M., Rauw G., Blomme R., Pittard J. M., Stevens I. R., Runacres M. C., 2005, *A&A*, 437, 1029
 De Becker M., Rauw G., Sana H., Pollock A. M. T., Pittard J. M., Blomme R., Stevens I. R., Van Loo S., 2006, *A&A*, submitted
 De Becker M., 2005, Ph.D. thesis, Université de Liège
 Dessart L., Crowther P. A., Hillier D. J., Willis A. J., Morris P. W., van der Hucht K. A., 2000, *MNRAS*, 315, 407
 Dessart L., Owocki S. P., 2003, *A&A*, 406, L1
 Domingo-Santamaría E., Torres D. F., 2006, *A&A*, 448, 613
 Dougherty S. M., Beasley A. J., Claussen M. J., Zauderer B. A., Bolingbroke N. J., 2005, *ApJ*, 623, 447
 Dougherty S. M., Pittard J. M., Kasian L., Coker R. F., Williams P. M., Lloyd H. M., 2003, *A&A*, 409, 217
 Dougherty S. M., Williams P. M., 2000, *MNRAS*, 319, 1005
 Dougherty S. M., Williams P. M., Pollacco D. L., 2000, *MNRAS*, 316, 143
 Dougherty S. M., Williams P. M., van der Hucht K. A., Bode M. F., Davis R. J., 1996, *MNRAS*, 280, 963
 Draine B. T., McKee C. F., 1993, *ARA&A*, 31, 373
 Duffy P., Kirk J. G., Gallant Y. A., Dendy R. O., 1995, *A&A*, 302, L21
 Dwarkadas V. V., Owocki S. P., 2002, *ApJ*, 581, 1337
 Eenens P. R. J., Williams P. M., 1992, *MNRAS*, 255, 227
 Eichler D., Usov V., 1993, *ApJ*, 402, 271
 Ellison D. C., Baring M. G., Jones F. C., 1995, *ApJ*, 453, 873
 Ellison D. C., Baring M. G., Jones F. C., 1996, *ApJ*, 473,

1029

Ellison D. C., Cassam-Chenaï G., 2005, *ApJ*, 632, 920

Ellison D. C., Decourchelle A., Ballet J., 2004, *A&A*, 413, 189

Ellison D. C., Decourchelle A., Ballet J., 2005, *A&A*, 429, 569

Ellison D. C., Drury L. O.'C., Meyer J.-P., 1997, *ApJ*, 487, 197

Ellison D. C., Jones F. C., Baring M. G., 1999, *ApJ*, 512, 403

Fegan S. J., Hall J., Vassiliev V. V., 2003, in *Proceedings of the 28th International Cosmic Ray Conference*, eds. T. Kajita, Y. Asaoka, A. Kawachi, Y. Matsubara & M. Sasaki, p.2847

Fermi, E., 1949, *Phys. Rev.*, 75, 1169

Figer D. F., Kim S. S., Morris M., Serabyn E., Rich R. M., McLean I. S., 1999, *ApJ*, 525, 750

Figer D. F., McLean I. S., Morris M., 1999, *ApJ*, 514, 202

Fullerton A. W., Massa D. L., Prinja R. K., 2006, *ApJ*, 637, 1025

Gayley K. G., Owocki S. P., Cranmer S. R., 1997, *ApJ*, 475, 786

Ghez A. M., et al., 2005, *ApJ*, 620, 744

Hartman R.C., Bertsch D.L., Bloom S.D. et al., 1999, *ApJS*, 123, 79

Henley D. B., 2005, PhD thesis, University of Birmingham, UK

Henley D. B., Stevens I. R., Pittard J. M., 2003, *MNRAS*, 346, 773

Herrero A., Puls J., Najarro F., 2002, *A&A*, 396, 949

Hill G. C., 2001, in Barthelemy C., ed., *Proc. XXXVI Rencontres de Moriond, Electroweak Interactions and Unified Theories*, <http://moriond.in2p3.fr/EW/2001/proceedings/> (astro-ph/0106064)

Hillas, A. M., 2005, *Journal of Physics G Nuclear Physics*, 31, 95

Hillier D. J., Miller D. L., 1999, *ApJ*, 519, 354

Hillier D. J., Lanz T., Heap S. R., Hubeny I., Smith L. J., Evans C. J., Lennon D. J., Bouret J. C., 2003, *ApJ*, 588, 1039

Horns D., 2005, *Phys. Letters*, B607, 225

Jardine M., Allen H. R., Pollock A. M. T., 1996, *A&A*, 314, 594

Jokipii J. R., 1987, *ApJ*, 313, 842

Kirk J. G., Duffy P., Gallant Y. A., 1996, *A&A*, 314, 1010

Kirk J. G., Heavens A. F., 1989, *MNRAS*, 239, 995

Koch H. W., Motz J. W., 1959, *Rev. Mod. Phys.*, 31, 920

Lipari P., 1993, *Astropart. Phys.*, 1, 195

Longair M. S., 1994, *High Energy Astrophysics*, Vol. 2 (2nd ed.; Cambridge: Cambridge Univ. Press)

Malkov M. A., Diamond P. H., Völk H. J., 2000, *ApJ*, 533, L171

Marchenko S. V., Moffat A. F. J., Vacca W. D., Côté S., Doyon R., 2002, *ApJ*, 565, L59

Marchenko S. V. et al., 2003, *ApJ*, 596, 1295

Mastichiadis A., 1996, *A&A*, 305, L53

Massa D., Fullerton A. W., Sonneborn G., Hutchings J. B., 2003, *ApJ*, 586, 996

Mayer-Hasselwander H. A., et al., 1998, *A&A*, 335, 161

Melrose D. B., Crouch A., 1997, *PASA*, 14, 251

Mewe R., Kaastra J. S., Liedahl D. A., 1995, *Legacy*, 6, 16

Meyer J.-P., Drury L. O'C., Ellison D. C., 1997, *ApJ*, 487, 182

Moffat A. F. J., et al., 2002, *ApJ*, 573, 191

Mullan D. J., Waldron W. L., 2006, *ApJ*, 2006, 637, 506

Muno M. P., et al., 2004, *ApJ*, 613, 326

Naito T., Takahara F., 1995, *MNRAS*, 275, 1077

Nodes C., Birk G. T., Gritschneider M., Lesch H., 2004, *A&A*, 423, 13

Orth C. D., Buffington A., 1976, *ApJ*, 206, 312

Oskinova L., 2005, *MNRAS*, 361, 679

Owocki S. P., Castor J. I., Rybicki G. B., 1988, *ApJ*, 335, 914

Owocki S. P., Cohen D. H., 2006, *ApJ* accepted

Ozernoy L. M., Genzel R., Usov V. V., 1997, *MNRAS*, 288, 237

Quataert E., Loeb A., 2005, *ApJ*, 635, L45

Pacholczyk A. G., 1970, *Radio Astrophysics* (San Francisco: W. H. Freeman and Company)

Perley R. A., Taylor G. B., 2003, in *The VLA Calibrator Manual* (<http://www.aco.nrao.edu/~gtaylor/calib.html>)

Petschek H. E., 1964, in *The Physics of Solar Flares*, ed. W. N. Ness, NASA SP-50, 425

Pittard J. M., Corcoran M. F., 2002, *A&A*, 383, 636

Pittard J. M., Dougherty S. M., Coker R. F., O'Connor E., Bolingbroke N. J., 2006, *A&A*, 446, 1001

Pittard J. M., Stevens I. R., 2002, *A&A*, 388, L20

Pittard J. M., Stevens I. R., Williams P. M., Pollock A. M. T., Skinner S. L., Corcoran M. F., Moffat A. F. J., 2002, *A&A*, 388, 335

Pollock A. M. T., Corcoran M. F., Stevens I. R., 2002, in Moffat A. F. J., St-Louis N., eds, *ASP Conf. Ser.* 260, 537

Pollock A. M. T., Corcoran M. F., Stevens I. R., Williams P. M., 2005, *ApJ*, 629, 482

Pope M. H., Melrose D. B., 1994, *PASA*, 11, 175

Priest E., Forbes T., 2000, "Magnetic Reconnection: MHD Theory and Applications", Cambridge University Press, UK

Raga A. C., Velázquez P. F., Cantó J., Masciadri E., Rodríguez L. F., 2001, *ApJ*, 559, L33

Rakowski C. E., 2005, *Adv. Space Res.*, 35, 1017

Reimer A., Pohl M., Reimer O., 2006, *ApJ*, 644, 1118

Repolust T., Puls J., Herrero A., 2004, *A&A*, 415, 349

Rockefeller G., Fryer C. L., Baganoff F. K., Melia F., 2005, *ApJ*, 635, L141

Romero G. E., Benaglia P., Torres D. F., 1999, *A&A*, 348, 868

Schlickeiser R., 1984, *A&A*, 136, 227

Schlickeiser R., 2002, *Cosmic Ray Astrophysics*, Springer, Berlin, Germany

Silich S., Tenorio-Tagle G., Rodríguez-González A., 2004, *ApJ*, 610, 226

Smith N., 2002, *MNRAS*, 337, 1252

Stevens I. R., Hartwell J. M., 2003, *MNRAS*, 339, 280

Stevens I. R., Pollock A. M. T., 1994, *MNRAS*, 269, 226

Torres D. F., Domingo-Santamaría E., Romero G. E., 2004, *ApJ*, 601, L75

Tuthill P. G., Monnier J. D., Danchi W. C., 1999, *Nature*, 398, 487

Van Hoof P. A. M., Martin P. G., Ferland G. J., 2000, in *ASP Conf. Ser.* 215, *Cosmic Evolution and Galaxy Formation: Structure, Interactions, and Feedback*, ed. J. Franco, L. Terlevich, O. Lopez-Cruz, & I. Arétxaga (San Fran-

cisco: ASP), 220
Van Loo S., Runacres M. C., Blomme R., 2006, A&A, 452, 1011
Varricatt W. P., Williams P. M., Ashok N. M., 2004, MNRAS, 351, 1307
Viotti R. F., Antonelli L. A., Rossi C., Rebecchi S., 2004, A&A, 420, 527
Völk H. J., Berezhko E. G., Ksenofontov L. T., Rowell G. P., 2002, A&A, 396, 649
White R. L., Becker R. H., 1995, ApJ, 451, 352
Williams P. M., 1996, RevMexAA (Ser. de Conf.), 5, 47
Williams P. M., van der Hucht K. A., Pollock A. M. T., Florkowski D. R., van der Woerd H., Wamsteker W. M., 1990, MNRAS, 243, 662
Williams P. M., Dougherty S. M., Davis R. J., van der Hucht K. A., Bode M. F., Setia Gunawan D. Y. A., 1997, MNRAS, 289, 10
Woosley S. E., Heger A., 2006, ApJ, 637, 914
Yusef-Zadeh F., 2003, ApJ, 598, 325
Yusef-Zadeh F., Nord M., Wardle M., Law C., Lang C., Lazio T. J. W., 2003, ApJ, 590, L103
Zhekov S. A., Skinner S. L., 2000, ApJ, 538, 808